A LARGE EDDY SIMULATION STUDY OF THE FORMATION OF DEEP CHLOROPHYLL/BIOLOGICAL MAXIMA IN UN-STRATIFIED MIXED LAYERS: THE ROLES OF TURBULENT MIXING AND PREDATION PRESSURE.

D. M. Lewis*[1] A. Brereton[2] & J. T. Siddons[1]

[1]*Department of Mathematics, University of Liverpool, M&O Building, Peach St, Liverpool L69 7Z*

Tel: *+44 151 794 4014.* Email: *D.M.Lewis@liverpool.ac.uk, J.T.Siddons@liverpool.ac.uk.*

[2]*National Oceanography Centre, 6 Brownlow Street, Liverpool L3 5DA*

Email: *ashbre@noc.ac.uk*

*Corresponding author

Abstract

Recent experimental measurements of fluorescence values and turbulent energy dissipation rates, recorded in weakly stratified boundary layers in the open ocean, have highlighted a significant correlation between the formation of deep chlorophyll maxima (*DCM*) and turbulent mixing. Specifically, the depth of many *DCM* are observed to lie below, but within about one standard deviation, of the point at which the energy dissipation rate profile reaches its maximum. This correlation of *DCM* and turbulent mixing is both exciting and curious, as conventional thinking tends to see the latter as a destructive rather than a constructive agent in regards to the formation of deep biological maxima (*DBM*), for which *DCM* data is usually interpreted as a proxy. In order to investigate this phenomenon, a 3D Large Eddy Simulation (LES) of the ocean boundary layer was combined with a generic NPZ type biological model, in order establish what mechanisms might be driving the experimental observations. Simulations of the LES-NPZ model, based upon various sets of generic biological parameters, demonstrate *DCM/DBM* formation occurs at normalised depths close to those seen in the experimental observations. The simulations support the hypothesis that the *DBM* are generated by a combination of zooplankton predation pressure curtailing phytoplankton growth near the surface, and a decline in the strength of the vertical mixing processes advecting nutrient through the boundary layer. In tandem these produce a region of the water column in which predation pressure is relatively low and nutrient aggregation relatively high, suitable conditions for *DBM* formation.

1. Introduction

The presence of deep (or sub-surface) chlorophyll/biomass maxima (*DCM/DBM*) observed in vertical fluorescence profiles is one of the most ubiquitous features of the world's oceans (Macías *et al*. 2008), and much research effort has been devoted to understanding the mechanisms behind their formation and dynamics (see Cullen 2015 for a comprehensive review of the subject). Observations of *DCM* are not just confined to the ocean boundary layer (e.g. Cullen 1982, Estrada *et al*. 1993, Letelier *et al*. 2004, Macías *et al.* 2013), but are a pervasive feature of the limnology of lakes too (Hamilton *et al*. 2010, White & Matsumoto 2012, Simmonds *et al*. 2015). Here the terminology *DCM* specifies a broad (10-20m) region of relatively high chlorophyll concentrations (but weak concentration gradients), usually to be found at or somewhat below the mixed layer depth. This should not be confused with the concept of a rapidly varying biological 'thin layer', confined to vertical scales of just a few metres (e.g. Dekshenieks *et al.* 2001, McManus *et al.* 2003 & 2005, Johnston *et al.* 2009 Benoit-Bird *et al.* 2009, Durham *et al.* 2009), which are usually found residing within the top 10m or so of the water column.

A number of different postulates have been advanced to attempt to explain both the formation of *DCM*, and the reasons as to why they are observed so frequently under many different hydrodynamic conditions. These include the presence of a nutricline, giving rise to increases in phytoplankton growth rates in certain preferential layers of the water column (Simmonds *et al.* 2015), or the physical accumulation of phytoplankton cells at boundary layer interfaces (Ruiz *et al*. 2004, Huisman *et al.* 2006), such as the thermo/pycnocline (Dekshenieks *et al.* 2001). One possible mechanism by which aggregations could form at such boundaries would be through the action of intense levels of shear instabilities disrupting the swimming motions and effectively trapping gyrotatic micro-organisms (Durham *et al*. 2009, Hoeckner-Martinez & Smyth 2012). A further alternative, highlighted by the

observational and numerical work of Fennel & Boss (2003), emphasizes what they term the "general compensation depth", a level at which the local phytoplankton growth rate is balanced out by losses due to zooplankton grazing and divergences of settling velocity. This emphasis on predation pressure through zooplankton grazing is important because the upper ocean mixing layer most conducive to high levels of phytoplankton growth (it usually encompasses the euphotic zone in which light levels are sufficient for photosynthesis) is turbulent, and turbulence levels significantly influence planktonic predation (e.g. Rothschild & Osborn 1988, MacKenzie & Kiørboe 1995, Lewis 2003, Galbraith *et al.* 2004, Lewis & Bala 2006 and references therein). Awareness of the rôle played by turbulence in the formation and sustenance of biological layers has recently been heightened by the publication of new observational evidence. This is derived from data recorded by sophisticated, next generation, instrumentation, which shows that turbulent mixing rates and biological layers are frequently correlated (Wang & Goodman 2010, Macías *et al.* 2013), highlighting that background turbulence has a potentially creative, as well as a destructive capacity in regard to biological aggregations. The observations of Macías *et al.* 2013 are particularly striking in this regard, and are discussed in a little more detail in Section 2. They provide both motivation and empirical support for the subsequent theoretical/computational analysis.

The question that now arises is how to go about investigating the creative and destructive capacity of boundary layer turbulence in regards to *DCM/DBM* production? The recent increase in instrumentation sophistication has been achieved hand-in-hand with ever increasing advances in both computational speed and storage capacity. This in turns enables one to contemplate the use of much more ambitious and extensive modelling methodologies than have been attempted hitherto. The most common means of modelling planktonic population dynamics has been through the utilization of some form of coupled nutrient-phytoplankton-zooplankton (NPZ) system of differential equations (e.g. Franks 1995,

Edwards *et al.* 2000, Franks 2002). Usually such models contain various simplified descriptions of nutrient uptake, phytoplankton growth and zooplankton predation built into their equations. To study the effects of turbulence requires a more sophisticated, coupled, biophysical model. Previously this has been attempted by adding in a vertical eddy diffusivity term into the NPZ system, which in effect creates a one dimensional (vertical) biological boundary layer model (Baird & Emsley 1999, Denman & Peňa 1999, Flierl & McGillicuddy 2002, Fennel & Boss 2003). However, the use of vertical eddy diffusivities in this way provides only a crude measure of the effects of water motion on the biology, particularly given that turbulence is, by definition, characterised by high levels of vorticity, which is fundamentally three dimensional in nature (Tennekes & Lumley 1972, McComb 1991, Lesieur 1997). Given the unquestioned advances in computational speeds in recent years, it seems reasonable to try and formulate something more powerful and sophisticated.

In Lewis (2005) the author attempted to devise such a model, building on ideas first formulated in the review article of Denman & Gargett (1995). This was achieved by employing a series of large-eddy simulations (LES) of ocean mixing layers, coupled together with a specially adapted NPZ model (specifically based upon the ideas of Baird & Emsley 1999) to describe the biological evolution in such an environment. LES captures the large scale features of a boundary layer flow extremely well and these are utilised to advect the biological fields in bulk. Although random, on small (planktonic) scales turbulent flows possess certain universal generic features, usually characterised by the local energy dissipation rate $\varepsilon(z)$ at a specified depth z. These generic features mean that the influence of the physical forcing on the population dynamics will conform to certain statistical norms, which can be estimated. Hence a knowledge of ε allows one to parameterise the coupling of the LES to the NPZ, to create a fully integrated, three dimensional, bio-physical model across all scales. The main details of the adaptations necessary to produce a combined LES-NPZ

model of the mixing layer were presented in Lewis (2005). In that work the behaviour of the (initially uniform) biological fields when subjected to a fixed level of wind forcing was investigated. These results were generally satisfactory, but computational limitations restricted the run times to no more than a day or so, severely restricting the interval during which significant heterogeneities in the biological fields might develop. Subsequent advances in computational capacity and processor speed now allow one to carry out runs over periods of days and weeks, giving the opportunity to investigate the potential for the development of aggregations over a number of biological cycles. In conjunction with the new experimental results starting to become available, the LES-NPZ model now provides a means of investigating the drivers of *DCM/DBM* production and dissipation to a much greater degree of precision than hitherto. The results and analysis of a number of such investigations (presented in Section 5) comprise the main body of this paper.

2. A brief summary of the observations of DCM recorded in the subsurface upper ocean as discussed in the paper by Macías *et al.* (2013).

Briefly the paper of Macías *et al.* (2013) (denoted by M13 subsequently) describes an extensive series of measurements recorded using a TurboMAP-L fast sampling (512Hz) probe (Doubell *et al.* 2009), which is capable of measuring conductivity, sea temperature, vertical shear and fluorescence on a resolution scale of the order of centimetres. Measurements were taken at four different marine environments (specifically a coastal upwelling region of the Alboran Sea off the east coast of Spain, in the tidally-dominated Strait of Gibraltar (Macías *et al.* 2008), a region of open ocean in the North Atlantic situated $\sim 34^0 30' \mathrm{N}, 8^0 30' \mathrm{W}$, and at a site just off the tip of the Antarctic Peninsula.) by allowing the probe to free-fall from the surface to a typical depth of 150m (so encompassing both the

upper wind driven mixed layer and the lower weakly stratified portion of the water column). The North Atlantic trials took place during the spring, but measurements from the other three sites were conducted during the summer months. At this time of year, *DCM* are very prevalent in polar and temperate latitudes. This is thought to be connected with the fact that in summer the levels of turbulent mixing are relatively low, leading to nutrient depletion and low phytoplankton growth in the upper mixed layer (Holm-Hansen *et al.* 2005). Estimates of (average) energy dissipation rate profiles $\varepsilon(z)$ were calculated from the vertical shear measurements recorded by the probe by means of the relation

$$\varepsilon(z) = \frac{15}{2}\nu\,\langle\frac{\partial u}{\partial z}\rangle^2\,, \qquad (1)$$

where ν is the kinematic viscosity (which is slightly temperature dependent but a value of $\nu = 10^{-6}\mathrm{m}^2\mathrm{s}^{-1}$ will be assumed throughout this work). M13 do point out that the sampling within the highly turbulent near surface region (where wind stresses and wave effects are at their maximum) may be somewhat problematic, since the TurboMAP-L probe needs to be sinking at an almost constant speed through the water column. Such conditions are only reached at depths 10-15m below the surface. The prevailing vertical stratification conditions were summarised by means of an average buoyancy frequency $N(z)$, determined by

$$N^2(z) = -\frac{g}{\rho}\langle\frac{\partial \rho}{\partial z}\rangle, \qquad (2)$$

where ρ is the water density. Measurements of both fluorescence $F(z)$ (measured in relative fluorescent units) and energy dissipation rate were fitted to standard Gaussian curves to create model depth profiles. Four such profiles, one from each of the locations mentioned above, superimposed on the respective raw data are shown in Fig.1. (These profiles are reproduced from those of Fig. S1 of M13.)

Amongst the many interesting features of these datasets, the most pertinent to this particular study is the relative position of the deep chlorophyll maximum DCM_{depth}, to the position $peak_{depth}$ at which the energy dissipation rate reaches its recorded maximum. Some 73% of the analysed $\varepsilon(z)$ profiles were termed 'positive', in the sense that they exhibited a sub-surface $peak_{depth}$. Of these 'positive' profiles, two thirds (31 out of 46 profiles) exhibited a DCM_{depth} situated below, but within one standard deviation of $peak_{depth}$. The average DCM_{depth} for these 'matching' (M13) profiles was located some 18m deeper than the corresponding $peak_{depth}$ values. In other words, the maximum fluorescence measurements were significantly correlated with negative (decaying) $\varepsilon(z)$ gradients within the upper ocean mixed layer. In the remaining 15 profiles this correlation was absent. The main difference between these latter mixing layers was their relatively high degree of stratification ($N^2 = 3.21 \pm 1.82 \times 10^{-3}\mathrm{s}^{-2}$), compared to the much lower values ($N^2 = 1.1 \pm 1.2 \times 10^{-3}\mathrm{s}^{-2}$) associated with the 'matching' profiles. These results are important because many theoretical explanations of the formation of heterogeneous phytoplankton concentrations begin with the premise that significant stratification is already present, and such conditions are a prerequisite for biological aggregations (especially thin layer formation e.g. Durham *et al*. 2009, Hoeckner-Martinez & Smyth 2012). But here is experimental evidence of intense DCM (typical values of the magnitude of DCM_{max} are between 2-6 times the background) forming in the absence of strong stratification. Usually the presence of a DCM correlates exactly with a corresponding deep biomass maximum DBM, although there is some experimental evidence (Longhurst & Harrison 1989, Pérez *et al.* 2006, Cullen 2015) that the latter can be displaced slightly below the former as the chlorophyll-to-carbon ratio increases with depth. However, this displacement usually occurs in relatively stable ocean boundary layers found in tropical waters, conditions which do not apply to any of the locations discussed in M13. Hence for these sites it is fair to assume that the measured DCM is equivalent to the DBM. So

the question arises, what causes the formation of these aggregations in the absence of significant stratification in the upper boundary layer?

M13 postulate that the existence of a DCM may be explained by the juxtaposition of two vertically opposing gradients of resources: light availability from the surface necessary for photosynthesis and vertical mixing of nutrient rich deep waters into the euphotic zone, creating an 'optimal window' for the formation of the DCM. This seems a highly plausible hypothesis, albeit one that is likely to be modulated by other factors. M13 highlight the possible rôle of cells sinking faster out of high turbulence zones and accumulating in low vorticity regions situated below $peak_{depth}$, a hypothesis supported by the experiments of Ruiz *et al.* (2004). Another potential regulatory factor is that of planktonic predation (summarised, somewhat loosely, as that of a generic zooplankton species feeding on a generic species of phytoplankton), which is known to be strongly dependent upon the level of background turbulence (Rothschild & Osborn 1988). This is another vertical gradient that augments those governing the availability of light and nutrients. Modern high speed computing resources means it is now quite possible to investigate and test such postulates much more systematically (and cheaply) than ever could be done using field trial data alone (vital though that remains). A necessary pre-requisite is the existence of suitable bio-physical models of the upper ocean boundary layer, which incorporate both the effects of wind-driven and surface wave generated turbulence, coupled with the biological drivers of plankton population dynamics. These are just the kind of bio-physical characteristics the LES-NPZ model is able to replicate.

3. A description of the LES-NPZ model

Conceptually, the biological part of the LES-NPZ model is little different from other three state NPZ models in the literature (e.g. Keifer & Atkinson 1984, Fasham *et al*. 1990, Edwards & Brindley 1996, and previous references cited). Three, non-dimensional, scalar fields

denoted by $N(\boldsymbol{x},t) = N^*/N_0$, $P(\boldsymbol{x},t) = P^*/P_0$ and $Z(\boldsymbol{x},t) = Z^*/Z_0$, representative of nutrient (specifically nitrate), phytoplankton and zooplankton (where N_0 in kg m^{-3}, P_0 and Z_0 in cells m^{-3} are suitable reference scales) are assumed to satisfy three advection diffusion equations of the general form

$$\frac{DN}{Dt} + \boldsymbol{U_S}.\nabla N = D_{TN}\nabla^2 N - N \text{ uptake by } P + N \text{ recycled from } P \text{ growth}, \quad (3)$$

$$\frac{DP}{Dt} + \boldsymbol{U_S}.\nabla P = D_{TP}\nabla^2 P + P \text{ growth from } N - P \text{ grazing loss}, \quad (4)$$

$$\frac{DZ}{Dt} + \boldsymbol{U_S}.\nabla Z = D_{TZ}\nabla^2 Z + Z \text{ growth grazing } P + Z \text{ mortality}. \quad (5)$$

Here $D/Dt \equiv \partial/\partial t + \boldsymbol{u}.\nabla$, and $\boldsymbol{u}(\boldsymbol{x},t) = [u,v,w] = [u_1,u_2,u_3]$ is the (resolved LES) turbulent velocity field. This provides the first component of the physical coupling to the biology and is derived from a spatially and temporally (over one wave period) averaged version of the full three dimensional Navier-Stokes equations. First derived by Craik & Leibovich (1976), these consist of the equations of continuity $\nabla.\boldsymbol{u} = 0$, momentum

$$\frac{D\boldsymbol{u}}{Dt} + f\widehat{\boldsymbol{k}} \times (\boldsymbol{u} + \boldsymbol{U_S}) = -\frac{\nabla p_S}{\rho_0} - g\frac{\rho'}{\rho_0} + \boldsymbol{U}_S \times \boldsymbol{\omega} + SGS\,, \quad (6)$$

and energy

$$\frac{D\theta}{Dt} + \boldsymbol{U}_S.\nabla\theta = SGS. \quad (7)$$

In (6) and (7), f is the Coriolis frequency, $\boldsymbol{U_S}$ the Stokes drift velocity, $\boldsymbol{\omega} = \nabla \times \boldsymbol{u}$ the vorticity, g is the acceleration due to gravity, $\theta(\boldsymbol{x},t) = \theta_r + \theta'(\boldsymbol{x},t)$ the temperature field, $\rho(\boldsymbol{x}) = \rho_0 + \rho'(\boldsymbol{x})$ the fluid density and $p_S = p + \rho_0[2\boldsymbol{u}.\boldsymbol{U}_S + |\boldsymbol{U}_S|^2]/2$ a generalized pressure term. The density is assumed to be proportional to the temperature, such that $\rho'/\rho_0 = \theta'/\theta_r$ and details of the values of these parameters, including the reference density ρ_0 and temperature θ_r, are given in Table 1. The Stokes drift velocity was estimated by assuming that the ocean consists of steady, monochromatic deep-water waves (Philips 1977),

which (for convenience) are directed along the x-axis (easterly direction). In which case $\boldsymbol{U}_S = (U_S e^{2kz}, 0, 0)$, where $U_S = \sigma k a^2$, a being the wave amplitude, k the wave-number and $\sigma = \sqrt{gk}$ the wave frequency (see Table 1).

The sub-grid scales (SGSs) used to close the equations are based on a standard Smagorinsky (1963) scheme in which the unresolved Reynolds stresses $\overline{u_i' u_j'}$ (where the overbar denotes the filtering operation) and buoyancy fluxes $\overline{u_i' \theta'}$ are related to the spatial gradients of resolved flow field, so that

$$\overline{u_i' u_j'} = -\nu_T S_{ij} = -\nu_T \left[\left(\frac{\partial u_i}{\partial x_j} + \frac{\partial u_j}{\partial x_i} \right) - \frac{2}{3} \delta_{ij} \frac{\partial u_k}{\partial x_k} \right], \qquad \overline{u_i' \theta'} = \frac{\nu_T}{Pr} \frac{\partial \theta}{\partial x_i}, \tag{8}$$

where ν_T is an eddy viscosity and Pr is a turbulent Prandtl number. Details of the choice of the eddy viscosity in terms resolved strain rate S_{ij} and a resolution scale L_0 (set to be 1m throughout) are discussed in Lewis (2005). Note the distinction between q', the unresolved part of a scalar quantity $q_{total} = \bar{q} + q'$, and q'' used later to denote a fluctuation in the LES resolved part $q(\boldsymbol{x}, t) = \overline{q(\boldsymbol{x}, t)} = \langle q \rangle + q''(\boldsymbol{x}, t)$, derived from eqs. 6-7. (In what follows $\langle q \rangle$ denotes $q(z, t) = \frac{1}{4XY} \int_{-X}^{X} \int_{-Y}^{Y} q(\boldsymbol{x}, t)\, dxdy$, the *instantaneou*s horizontal mean of a resolved quantity. Similarly $\langle q \rangle_T$ will denote $q(z) = \frac{1}{T} \int_0^T \langle q \rangle dt$, the *time averaged* horizontal mean, over a specified interval T.) For code verification purposes solutions of the velocity and temperature (pressure) fields were computed from equations (6-7) over a domain $120 \times 120\text{m}^2$ horizontally and to a simulation base depth $z_S = 33(50)\text{m}$, utilising a basic grid of $40 \times 40 \times 75(114)$ nodes. This implies a regular resolution scale of $\Delta x = \Delta y = 3\text{m}$ and $\Delta z = 0.45\text{m}$ (although the vertical resolution is staggered to give greater resolution near the sea surface). In the course of these investigations many different turbulent boundary layers were generated. Their characteristics will be distinguished by the values of the Stokes drift

velocity U_S, and the friction velocity U_*, which determines the strength of the wind forcing applied at the surface

$$\nu_T \frac{\partial u}{\partial z}\Big|_{z=0} = \frac{\tau}{\rho_0} = U_*^2. \quad (9)$$

Here τ is the surface wind stress, which was varied between simulations over a range of $2.25\text{-}25.0 \times 10^{-3}\mathrm{kgm^{-1}s^{-2}}$. This implies values of U_* lying between $1.5\text{-}5.0 \times 10^{-3}\mathrm{ms^{-1}}$, roughly equivalent to windspeeds $U_{10} = 1.2\text{-}4.0\ \mathrm{ms^{-1}}$ at a height of ten metres. The corresponding values of U_S are given in Table 1. All the boundary layers were made slightly convective, with a turbulent buoyancy flux of $\overline{w'\theta'} = -1.2 \times 10^{-6}\mathrm{Kms^{-1}}$ applied at the surface. Other boundary conditions imposed on the flow are horizontal periodicity, $w = 0$ at $z = 0$ and no slip at $z = -z_S$. Typically, the various boundary layers were spun up from rest for a period τ_{spin}~60000s until a quasi-equilibrium state was reached, before any biological fields were added. This marks time zero for the simulations proper. The physical characteristics governing the generation of a particular simulation will be denoted by its (U_*, U_S) number. So the notation $(U_*, U_S) = (3.5, 3.9)$ specifies a simulation in which $U_* = 3.5 \times 10^{-3}\mathrm{ms^{-1}}$ and $U_S = 3.9 \times 10^{-2}\mathrm{ms^{-1}}$ respectively. The corresponding Langmuir number $La = \sqrt{U_*/U_S}$, as defined by McWilliams et al. (1997), can also be used to classify the simulations.

The performance of the LES code was extensively tested by comparing its output with that of a similar code employed by McWilliams *et al*. (1997) to study Langmuir turbulence in the upper ocean boundary layer. Comparison profiles of horizontal currents, shear stresses, velocity variances and energy dissipation rates (Lewis 2005) showed excellent agreement across the mixing layer $z \in [-z_{ML}, 0]$. Here z_{ML} represents the mixing layer depth (e.g. de

Boyer Montégut *et. al.* 2004), which varies according to both the strength of the wind forcing and the local hydrography (density and/or temperature differences, usually measured from the surface). The main difference between the two codes is the incorporation by McWilliams *et al*. (1997) of a stably stratified region below z_{ML} extending to a depth of $z \approx -3z_{ML}$. By contrast, the LES-NPZ model does not feature any such stratification. This raises a problem with the use of the terminology 'mixing-layer depth' when applied to these simulations, since the hydrographical features that help regulate its position are absent. So for this work an alternative concept of turbulent or Ekman depth, will also be used. This depends purely on the mixing properties of the flow and is defined by Coleman *et al.* (1990) to be $z_{TD} = U_*/f$. In practice z_{TD} will be larger than z_{ML}, since the latter is constrained by the hydrographic features of the flow not incorporated into these simulations (Pearson *et. al.* 2015). A rough equivalence would be closer to $z_{ML} \sim z_{TD}/2$. From a review of the relevant literature, Garratt (1992) suggests $z_{ML} \sim 0.2 - 0.4 z_{TD}$ for weakly stratified layers, but the inclusion of the Stokes drift term in (6) means that the mixing layer of these simulations is certain to be somewhat deeper than this. Since the velocity field is virtually zero below z_{TD}, whilst the majority of M13's measurements of DCM are found within weakly stratified mixed layers at depths significantly above z_{TD} (the turbulent mixing, although declining, is still a prevalent feature in Fig. 1), the lack of a stratified base to the computational domain is not a serious issue for this work.

Figs. 2-4 show some typical flow parameters derived from samples of these simulations. Fig. 2 shows the depth dependence of the mean (LES) velocities $\langle u \rangle_T$ and $\langle v \rangle_T$ derived from a $(U_*, U_S) = (3.5, 3.9)$ simulation after a time $T = T_{sim} \sim$ 20-25 days. Typically, except very near the surface, the mean flow is directed in a south-southwest direction, with both $\langle u \rangle_T$ and $\langle v \rangle_T$ negative. The effect of the Stokes drift term is to deflect the mean current anticlockwise - away from the easterly wind direction - considerably beyond the 45^0 degrees predicted by

classical Ekman boundary layer theory (Lewis & Belcher 2004). Fig. 3a shows a comparison of the mean velocity variance profiles $\langle u''^2\rangle_T, \langle v''^2\rangle_T$ and $\langle w^2\rangle_T$ taken from the same simulation. (N.B. $w \equiv w''$, since $\langle w\rangle = 0$.) A feature of these results is the relatively large scale of the vertical $\langle w^2\rangle_T$, as opposed to the horizontal $\langle u''^2\rangle_T + \langle v''^2\rangle_T$ turbulent mixing. Physically this is a manifestation of the formation of Langmuir cells, a series of counter rotating vortices aligned with the wind direction driven by the interaction of the wave field stretching and tilting the vertical vorticity field (Teixeira & Belcher 2002). From a biological point of view this enhanced mixing helps to ensure any nutrient resources, drawn from the deep ocean by large scale up-welling events, will be distributed quickly and uniformly throughout the mixing layer.

The other key physical parameter which encapsulates the mixing is the mean energy dissipation rate $\varepsilon(z)$ highlighted earlier (q.v. eq. 1 and Fig. 1). Fig. 4 shows some profiles of $\varepsilon(z)$, derived by balancing the (steady) resolved scale turbulent kinetic energy budget (McWilliams *et al.* 1997, Lewis 2005 eq.11, Polten & Belcher 2007), extracted from the $(2.0, 2.2)$, $(3.5, 3.9)$ and $(5.0, 5.6)$ simulation datasets over a period of $T \approx 1$ day. This involves combining terms such as Stokes, shear & buoyancy production, pressure working, turbulent transport and SGS dissipation. Near the surface $\varepsilon(z)$ shows significant variation, by roughly a factor of five in magnitude as U_* increases, but at greater depths the differences are far less evident. Notice too that the $\varepsilon(z)$ profiles often exhibit small secondary maxima, usually lying between about 5-15m below the surface. Such secondary maxima are a feature of these wind and wave driven Langmuir boundary layers. They can be explained by a comparison with the velocity variance profiles of Fig. 3a. Whilst the horizontal $\langle u''^2\rangle_T + \langle v''^2\rangle_T$ mixing component declines uniformly, this can sometimes be offset by vertical $\langle w^2\rangle_T$ component which initially increases near the surface, giving rise to the small secondary maxima in $\varepsilon(z)$. Comparing the profiles derived from these numerical simulations with the

experimental measurements of $\varepsilon(z)$ recorded by M13 (see Fig. 1), one can see that the values all lie in a broadly similar $10^{-7} - 10^{-6}\mathrm{m}^2\mathrm{s}^{-3}$ range. The main distinction is that for the numerical simulations the peak dissipation rate lies at the surface, where the wind and wave forcing are at their most intense, whilst in the experimental results the $peak_{depth}$ lies somewhat deeper. Careful inspection of all the low stratification profiles recorded off Spain and Gibraltar (e.g. Profiles 6 & 21 in Fig. 1) shows that the mean $peak_{depth}$ occurs at a relatively shallow 28.9m (M13 Table S1). In addition, most of these profiles exhibit dissipation values between $1 \times 10^{-7} - 2 \times 10^{-6}\mathrm{m}^2\mathrm{s}^{-3}$ at depths 10-15m below the surface, similar to those seen in the numerical simulations. The profiles recorded at the North Atlantic and Antarctic Peninsula sites (e.g. Profiles 28 & 31 in Fig.1) are somewhat different, exhibiting much deeper values of $peak_{depth}$~70m. The probable reason for these large sub-surface peaks is an increase in the energy dissipation rate at the mixed layer/thermocline boundary. Observations of increased energy dissipation rates within the thermocline have been recorded (e.g. Moum & Osborn 1986) and are believed to be result of the action of internal wave scattering due to buoyancy fluctuations (Gregg 1989). However, the magnitude of this increased mixing generally lies within the range $10^{-10} - 10^{-9}\mathrm{m}^2\mathrm{s}^{-3}$, which is rather too small to account for peaks shown in Fig. 1 and there may be other factors at work (see section 5a). In any event this should not distract from the main feature of *all* the profiles, namely the pattern of *DCM* formation at depths where $\varepsilon(z)$ is in sharp decline, which is motivation for this work.

The biological source/sink terms making up the right-hand sides of equations (3-5) are inspired by the work of Baird & Emsley (1999) and discussed in detail in Lewis (2005), so only a brief resumé is included here. Table 2 lists the main numerical values of the various biological parameters that appear in these terms. The nutrient uptake term in (3) is given by

$$N\ uptake\ by\ P = 4\pi r_P Sh(\varepsilon, z) D_N N(\boldsymbol{x}, t) \left[1 - \frac{R_{N_0}(z)}{R_N^{max}} N(\boldsymbol{x}, t)\right] P^*(\boldsymbol{x}, t), \quad (10)$$

provided (10) is positive, otherwise it is set to zero. This reflects the balance between nutrient uptake by means of turbulent diffusion and the limitations brought about by the nitrate storage capacity of an average cell. Here r_p is a typical phytoplankton cell radius, Sh a non-dimensional turbulent Sherwood number, D_N the molecular diffusivity of nitrate and $R_{N_0}(z)/R_N^{max}$ is the ratio of the nitrate storage capacity of the cell to its maximum potential storage capacity. The value of $R_{N_0}(z)$, assuming a background ambient nitrate concentration level N_0 set to be 2.8×10^{-5}kg m^{-3} (Fasham et al. 1990), can be established using a mass balance equation (Baird *et al*. 2001), as discussed in Lewis (2005). The R_N^{max} parameter was set to a value of $3s_N$ where s_N (kg cell^{-1}) is a nitrate stoichiometry coefficient quantifying the minimal amount of nitrate needed for a cell to be viable. Whenever the background concentration $N(\boldsymbol{x}, t)$ greatly exceeds N_0 then nutrient satiation sets in, at which point diffusion into the cell ceases. For the simulations results presented in Section 5 the value of $R_{N_0}(z)/R_N^{max} \approx 0.5$, which means that uptake ceases when the background nutrient concentration $N(\boldsymbol{x}, t) > 2$. The physical forcing influences the scale of (10) in two ways. Directly, through the dependence of Sh on ε, and indirectly through the effects of the turbulent mixing on the nutrient distribution. In practice the direct influence of ε on Sh is weak, since r_P is usually less than the Kolmogorov length scale $(\nu^3/\varepsilon)^{1/4}$, meaning that Sh varies little from unity across the boundary layer. The indirect influence of ε on (10), as manifested through the nutrient distribution is far more important, and will form part of the investigation carried out in Section 5.

The nitrate recycled and phytoplankton growth terms employed in (3) and (4) are essentially analogues of each other and depend significantly on the scale of (10). In the model they are given by

$$Nitrate\ recycled = (1-\beta_E)\frac{s_N P^*(\boldsymbol{x},t)}{N_0}\mu_P^{max} e^{\alpha z}\min\left[1, \frac{R_{N_0}(z)}{R_N^{max}}N(\boldsymbol{x},t)\right], \tag{11}$$

$$P\ growth = \beta_E \min\left[1, \frac{R_{N_o}(z)}{R_N^{max}}N(\boldsymbol{x},t)\right] e^{\alpha z}\mu_P^{max} P(\boldsymbol{x},t). \tag{12}$$

Equation (12) encapsulates the fact that a phytoplankton species can potentially reproduce at its maximum growth rate μ_P^{max} under ideal conditions; but this is regulated by the available light intensity for photosynthesis, which is assumed to decay exponentially with depth (α is the light attenuation coefficient for water), and the cellular reserves of nitrate currently available (see Baird & Emsley (1999) for more on the details underpinning these terms). Other factors can also inhibit phytoplankton growth efficiency and their effects are represented by the dimensionless parameter $\beta_E \in [0,1]$. These growth inefficiencies (cell death and decay) usually lead to a recycling of nitrate back into the water column, a process which is summarised by equation (11). The usual initial condition employed in these simulations will be to fix $N(\boldsymbol{x},0) = 1$, in which case the recycling term is about ten times smaller than the uptake term (10).

The loss of phytoplankton to zooplankton grazing and the zooplankton growth rate terms used in (4) and (5) are also analogous. In the model they appear as

$$P\ grazing\ loss = Z^*(\boldsymbol{x},t)P(\boldsymbol{x},t)I(R,T_R,\varepsilon,\sigma_Z)\,, \tag{13}$$

$$Z\ growth = \min[\mu_Z^{max}, YP^*(\boldsymbol{x},t)I(R,T_R,\varepsilon,\sigma_Z)]Z(\boldsymbol{x},t). \tag{14}$$

Here $I(R,T_R,\varepsilon,\sigma_P)$ is representative of a predation rate integral (units $\mathrm{m^3 s^{-1}}$) defined explicitly in Lewis & Pedley (2001 eqs. 16-17), evaluated over a range $[0,R]$, where R is the

contact radius of the zooplankton predator. This parameter is the maximum distance over which it can perceive its prey (R~1-40 $\times 10^{-3}$m) and in Lewis & Pedley (2001) it is assumed to be spherically symmetric for mathematical simplicity. In reality, most predators possess a much narrower conical perception field, the ramifications of which are discussed in Lewis (2003), Lewis & Bala (2006 & 2008). Loosely $I(R, T_R, \varepsilon, \sigma_Z)$ estimates the predation rate of the predator from its encounter rate (Rothschild & Osborn 1988), times its capture efficiency. The latter is governed by parameters such as a predator's reaction time T_R, its swimming or pursuit speed σ_Z and level of turbulence summarised by ε. Turbulence always enhances encounter rates by advecting more prey particles into the predator's vicinity, but in certain instances can lead to the suppression of the predation rate, because it makes the act of actually capturing prey more problematic. In this work the zooplankton predators are relatively small r_Z~$10^{-5} - 10^{-4}$m, and their corresponding swimming speeds σ_Z~$5 - 20 \times 10^{-4}\mathrm{ms}^{-1}$ are an order of magnitude smaller than the mixing velocity scales found in the upper boundary layer (Fig. 2). Consequently swimming is not included directly into the advection terms in (5) because it would be too small to influence the spatial distribution of the zooplankton. Potentially, swimming could make a significant impact at depths close to the mixing layer boundary where ε falls off rapidly and *DBM* are observed. This is particularly true of the predation term, which falls to zero in the absence of any advective or swimming motions. On balance this would a fairly unlikely scenario, but for illustrative purposes non-swimming predators will feature in some of the simulations (cf. Figs. 14 & 16) carried out here. The specific ideas as to how these competing factors are formulated into the integrand of $I(R, T_R, \varepsilon, \sigma_Z)$, are discussed in Lewis & Pedley (2001). Fig. 5a shows some profiles of the predation rate $I(R, T_R, \varepsilon, \sigma_Z)$ for a relatively efficient ($T_R = 5$s) non-swimming predator, possessing a contact radius $R = 2 \times 10^{-3}$m, over a range of windspeeds ($U_* =$ 2.0-5.0 $\times 10^{-3}\mathrm{ms}^{-1}$). Generally an efficient predator benefits from increasing levels of

turbulent mixing, since its encounter rate goes up leading to more prey captures. This is reflected in Fig. 5a which exhibits a steady increase of predation rate with windspeed. The benefit is particularly marked near the surface where ε is at its largest, q.v. Fig. 4. By contrast increased turbulent mixing can be detrimental to the predation rate of an inefficient predator ($T_R = 15\text{s}$), such as the one illustrated by the profiles in Fig. 5b. In these instances, the comparatively high relative velocities found near the surface means the predator has to react faster than T_R in order to capture prey moving into its vicinity. This it is unable to do, leading to a drop in its overall predation rate. The predation rate determines both the decline in the general phytoplankton population through grazing (13), and the zooplankton growth rate (14). The latter is regulated by the yield Y of new predator cells per prey cell captured, and is also restricted never to exceed a fixed maximum zooplankton growth rate μ_Z^{max}, theoretically attainable under ideal conditions.

The biological part of the model is closed by assuming that the zooplankton growth rate is limited by a simple constant mortality term of the form

$$Z\ mortality = \mu_{Z\ death} \frac{Z^*(\boldsymbol{x}, t)}{Z_0}. \qquad (15)$$

The mortality rate $\mu_{Z\ death}$ is a purely biological parameter independent of ε. Its importance stems from the fact that it regulates the period of oscillations of the planktonic P/Z populations within the model (see Section 4). The diffusion coefficients in (3-5) are calculated from the eddy viscosity by means of a turbulent Schmidt number

$$D_{T\Gamma} = \frac{\upsilon_T(\boldsymbol{x})}{Sc_{turbulent}} \qquad (\Gamma = N, P, Z). \qquad (16)$$

The Schmidt number cannot be too large as it is regulated by the LES resolution scale and one cannot expect to resolve the scalar fields down to a finer level than that can be achieved

for the velocity fields. A proposal made by Sullivan *et al*. (1994) and adopted in Lewis (2005) was to prescribe $Sc_{turbulent}$ in the form

$$Sc_{turbulent} = \frac{1}{(1 + 2\,L_0/\Delta)}, \tag{17}$$

where $\Delta^3 = (3\Delta x/2)(3\Delta y/2)\Delta z$. For the simulations discussed here $Sc_{turbulent} \approx 1/2$, a value compatible with L_0 scale which prescribes the resolution of the LES velocity field.

Equations (3-5) are solved subject to certain prescribed boundary conditions on the biological fields. Horizontally, periodic boundary conditions were imposed. Vertically, zero surface flux conditions are (usually) imposed for each field, whilst at $z = -z_S$ certain prescribed fluxes into the simulation domain were enforced. For the majority of the simulations presented here the vertical boundary conditions satisfied

$$\left.\frac{\partial \Gamma}{\partial z}\right|_{z=0} = 0, \qquad \frac{\upsilon_T}{Sc_{turbulent}} \left.\frac{\partial \Gamma}{\partial z}\right|_{z=-z_S} = \langle w\Gamma \rangle, \qquad (\Gamma = N, P, Z). \tag{18}$$

In the case of the planktonic fields, $\Gamma = P$ and Z, deceased cells were assumed to sink, under gravity, out of the simulation domain at a rate governed by a settling velocity U_{sink} (Lewis 2005). This fixes $\langle w\Gamma \rangle = U_{sink}\phi_\Gamma^{dead}\Gamma_{-z_S}$, where ϕ_Γ^{dead} is the (small) proportion of deceased cells out of the total population. The boundary conditions imposed on the nitrate field were more flexible. In general wind, tidal and other driving forces instigate upwelling motions that circulate nutrient rich water from the deep ocean through the mixing layer. So one would expect nitrate levels in the mixing layer to remain relatively constant, as losses through uptake by the phytoplankton for photosynthesis will be quickly replenished via this source. Hence a positive flux of nitrate into the simulation domain was invariably imposed. Williams and Follows (1998) suggest this background flux should be $\sim 2 \times 10^{-8}$ mol N $\mathrm{m^{-2}s^{-1}}$, which is roughly equivalent to $\langle w\mathrm{N}^* \rangle = -2.8 \times 10^{-10}\mathrm{kg\ m^{-2}s^{-1}}$. This figure was taken as

representative of the background nutrient replenishment flux from the deep ocean into the boundary layer. However, in instances where $z_S \gg z_{TD}$, introducing replenishment nutrient at the base is not very useful, since there is little or no mixing to advect it through the boundary layer. To overcome this problem, simulations were also conducted in which the replenishment flux was imposed at the surface ($z = 0$) instead. Such a *surface* nutrient surge could be driven by a significant river run off event, iron seeding experiments or even ash from a volcanic eruption (Frogner *et al.* 2001). This allows one to investigate what changes (if any) occur to the DCM/DBM characteristics when the replenishment nutrient is added at alternative depths subject to radically different turbulent mixing regimes.

4. Model verification and the influence of boundary layer structure on the Biological Dynamics

The full version of the LES-NPZ model seeks to summarise the effects of a number of different physical and biological drivers on the planktonic populations. It depends upon many different parameters, not all of which are critical in determining the evolution of the biology. To determine which terms are important and explore a suitable parameters space for the biological variables, a greatly simplified version of the NPZ model described above was developed with all the advection/diffusion terms and boundary layer structure removed. This simplified NPZ model reduces to the formulism

$$\frac{dN}{dt} = eP(t)\min\big(1, hN(t)\big) - d[1 - hN(t)]N(t)P(t) \times H\{1 - hN(t)\},$$

$$\frac{dP}{dt} = a\min\big(1, hN(t)\big)P(t) - bP(t)Z(t), \qquad (19\text{ a,b,c})$$

$$\frac{dZ}{dt} = Z(t)\min\big(\mu_Z^{max}, cP(t)\big) - \mu_{Z\,death}Z(t),$$

where $H\{x\}$ is the Heaviside step function ($H\{x\} = 1$ if $x \geq 0$ and zero if $x < 0$) and the other constants are given by

$$a = \beta_E \mu_P^{max}, \qquad b = I(R, T_R, \sigma_Z) Z_0, \qquad c = Y P_0 I(R, T_R, \sigma_Z),$$

$$d = 4\pi r_P Sh D_N P_0, \qquad e = (1 - \beta_E) \frac{s_N P_0}{N_0} \mu_P^{max}, \quad \& \quad h = \frac{R_{N_0}}{R_N^{max}}. \tag{20}$$

These terms no longer exhibit any dependency on depth z or turbulent mixing ε, which are features of the full LES-NPZ model. In this reduced form equations (19-20) are sufficiently simplified to allow some qualitative analysis of their behaviour. Assuming $hN(t) < 1$ and $cP(t) < \mu_Z^{max}$, (the most common scenario) the equations possess a single co-existence equilibrium point in positive phase space, situated at

$$(N_{EQ}, P_{EQ}, Z_{EQ}) = \left(\left(\frac{1}{h} - \frac{e}{d} \right), \frac{\mu_{Z\ death}}{c}, \frac{ah}{b} \left(\frac{1}{h} - \frac{e}{d} \right) \right) \approx \left(\frac{1}{h}, \frac{\mu_{Z\ death}}{c}, \frac{a}{b} \right). \tag{21}$$

Employing some fairly typical biological parameters, as listed in Table 2, one finds $h^{-1} > 10ed^{-1}$, hence the approximation made in (21). Linearised stability analysis of the community matrix of partial derivatives at this equilibrium point yields three eigenvalues of the form

$$(\lambda_1, \pm\lambda_2) \approx \left(\frac{d\mu_{Z\ death}}{c}, \pm \mathrm{i}\sqrt{a\mu_{Z\ death}} \right). \tag{22}$$

These eigenvalues give rise to three solution branches near (N_{EQ}, P_{EQ}, Z_{EQ}), one of which is an exponentially increasing on a time scale of $\tau_{exp} = c/d\mu_{Z\ death}$, whilst the remaining two associated branches give rise to oscillatory solutions for the (P, Z) fields on a timescale $\tau_{oscil} = 2\pi/\sqrt{a\mu_{Z\ death}}$. Based upon the biological parameters specified in Table 2

(specifically for those used in Fig. 6) one finds that $\tau_{oscil} \approx 10.5$ days whilst $\tau_{exp} \approx 43$ days. So this analysis suggests that if the initial populations happen to lie close to $\left(N_{EQ,}P_{EQ}, Z_{EQ}\right) \approx (1.56, 0.43, 0.85)$, then (P, Z) will oscillate regularly about their equilibrium values at a relatively rapid frequency $\sim 1/\tau_{oscil}$, whilst growing relatively slowly over the longer time scale τ_{exp}. However, this conclusion is slightly deceptive because the nutrient uptake term will shut down if ever N gets too large and cells become satiated (when $hN > 1$ in 19a). In such circumstances the predicted growth branch actually manifests itself as a *decay* branch, over the same long timescale τ_{exp}. This means that the (P, Z) populations simply oscillate regularly, whilst the nutrient concentration exhibits a net depletion, brought about by funding of the new P growth. Qualitatively, this kind of behaviour is illustrated in Fig. 6, which shows the evolution, over a period of 25 days, of the normalised Phytoplankton-Zooplankton-Nitrate fields, starting from initial values of $(N, P, Z)_{t=0} = (1.0, 0.5, 0.5)$. Oscillations in the (P, Z) fields over a timescale close to the predicted $\tau_{oscil} \approx 10.5$ days are apparent, whilst the N field decays relatively slowly from its initial value, since there is no mechanism for nutrient replenishment in the simplified NPZ model. Note too how the peaks in the Z field always lag a few days behind those of the phytoplankton concentration. This kind of behaviour is generic to other NPZ models, e.g. Baird & Emsley (1999), Edwards *et al.* (2000), Franks (2002).

In the simulations of the full LES-NPZ model which follow, the evolution of the P and Z-fields exhibits qualitatively similar oscillatory behaviour to that illustrated in Fig. 6. The period of the oscillations in the mixing layer always lies close to the value set by τ_{oscil}, except in those instances when the initial conditions $(P, Z)_{t=0}$ differ significantly from the equilibrium values $\left(P_{EQ,}, Z_{EQ}\right)$. The default values of $(P, Z)_{t=0} = 0.5$ usually employed are close enough to equilibrium for oscillatory behaviour to commence immediately. The

incorporation of turbulent mixing brings about some quantitative changes in the biological dynamics. Firstly the peak concentrations are somewhat reduced and smoothed out compared to those shown in Fig. 6 (typically by around 40% or so). The biological parameters in the simplified model are set appropriately for conditions at the surface $z = 0$, but in reality no phytoplanktonic cell will reside so close to the surface all the time and as a result its growth will be retarded by a lack of light when carried deeper into the boundary layer. This is counter-acted, to some extent, by the reduction in zooplankton predation pressure as one descends deeper into the boundary layer. The combination of these effects reduces the peak concentration scales. Secondly, as will be seen in many of the simulations, the turbulent mixing does not extend uniformly across the entire simulation domain. This means a cell initially situated somewhere near the top of the mixing layer has a higher probability of residing near the surface for longer periods and replicating more frequently than a cell initially residing below the mixing depth. (Since it experiences greater exposure to elevated light levels.) This effect gradually manifests itself in a visible lag in the intervals separating successive concentration peaks at different depths. The nutrient flux boundary condition (18) is sufficient to replenish nutrient losses due to phytoplankton growth, so the decline in nutrient concentration exhibited in Fig. 6 is not a feature of the full LES-NPZ model.

5. Studies of *DCM/DBM* formation and characteristics using the LES-NPZ model

Before looking in more detail at those bio/physical parameters which most influence the formation of *DCM/DBM*, it is worth pointing out some generic features common to all the LES-NPZ simulations results reported here. Each boundary layer is generated by means of the fixed wind forcing boundary condition (9), summarised by its (U_*, U_S) parameters. Typically a boundary layer is spun up from rest and the respective (U_*, U_S) forcing applied so that it relaxes into a state of quasi equilibrium, a process which takes about τ_{spin}~60000s. It

is at this point the mean $\varepsilon(z)$ profiles are estimated and these appear alongside the biological profiles in the figures that follow. Knowledge of $\varepsilon(z)$ allows one to calculate the biophysical coupling terms that appear in (3-5). The whole process is then repeated, but this time the onset of quasi-equilibrium is the signal for the biological fields to be introduced into the boundary layer. Biological evolution (usually) commences from an initial distribution $(N, P, Z)_{t=0} = (1.0, 0.5, 0.5)$, uniformly applied both horizontally and vertically. The biological fields are then allowed to evolve for a period $T_{sim}\sim$ 20-25 days, in accordance with the biological parameterisations set out in Table 2.

The choice of simulation time period $T_{sim}\sim$ 20-25 days is driven primarily by biological considerations. One needs to allow the biological fields to replicate through at least a couple of reproductive cycles. These values of T_{sim} are somewhat larger than τ_{pred} the predictability timescale of the LES. The latter is the time by which imperfections brought about by not resolving down to the smallest scales propagate through the eddy hierarchy to produce significant contamination of the large scale motions (see Lesieur 1997 Chapter XI-XII). For this work $\tau_{pred} \approx 25T_E = 25 \times$ large-eddy turnover scale ≈ 1.5 days. This does not invalidate the methodology, because a LES computed over times $T_{sim} > \tau_{pred}$ is still a statistically realistic representation of an actual flow, but one that is in the process of being advected as a complete body of water from its original position (as would happen under the action of a large scale current encompassing a much greater volume than the typical $120 \times 120 \times 33$ or 50m^3 domains used here). It is important that the flow statistics generated by the LES remain roughly stable over a simulation time period. Fig. 3b shows the evolution of the mean velocity variance $\langle u''^2 \rangle_T$ profile over a $T_{sim} = 23$ day period, taken from a representative $(U_*, U_S) = (5.0, 5.6)$ simulation. As one can see the variance remains almost

constant throughout, and this scenario applies for both the $\langle v''^2 \rangle_T$ and $\langle w^2 \rangle_T$ variances too. So the basic statistics are sufficiently robust for meaningful conclusions to be drawn.

5a) Sensitivity to wind forcing.

The first set of simulations were designed to investigate the sensitivity of *DCM/DBM* formation to wind forcing. To achieve this, three different wind driven boundary layers (each with a simulation depth $z_S = -50\text{m}$) were spun up, with parameter settings $(U_*, U_S) = (2.0, 2.2), (3.0, 3.3)$ & $(4.0, 4.4)$. These values are representative of low, intermediate and strong wind forcing regimes respectively (the terminology 'strong' is only comparative, since it represents a windspeed of only around 4ms^{-1}). Figs. 7a-c show the energy dissipation rate profiles for each of the three boundary layers in turn, alongside the corresponding profiles of zooplankton predation. Derived from the initial spin up run, these average profiles remain fixed throughout the subsequent biological simulation. The dissipation profiles show a progressive increase in the near surface maximum dissipation rates (0.65-2.0$\times 10^{-7}\text{m}^2\text{s}^{-3}$) with wind forcing, and a corresponding deepening of the mixing layer. In each case the dissipation rate falls to (almost) zero around about half the turbulent depth $\approx z_{TD}/2$, equivalent to 10, 15, & 20m respectively. The predation rate profiles $I(R, T_R, \varepsilon, \sigma_Z)$ are calculated for a relatively large predator (length scale $r_Z = 3 \times 10^{-4}\text{m}$), possessing a spherical perception field of radius $R = 1.3 \times 10^{-2}\text{m}$, with an average swimming speed $\sigma_Z = 2 \times 10^{-4}\text{ms}^{-1}$, reacting in a time $T_R = 5\text{s}$ (see Table 2). These profiles are all fairly similar near the surface (as T_R is only moderately fast, the predator cannot benefit from the increase in prey contacts brought about by the highest surface dissipation rates), falling away at different rates, before levelling off ~$10^{-7}\text{m}^3\text{s}^{-1}$ near $z_{TD}/2$. Since $\varepsilon(z < z_{TD}/2) \approx 0$ and the flow is relatively quiescent, the predator is forced to rely on its swimming capabilities alone in order to find prey. This means the predation rate is almost constant for $z < z_{TD}/2$.

Figs. 8a-c show the corresponding evolution of the biological (N, P, Z) profiles over the simulation time T_{sim}, assuming a maximum (surface) phytoplankton growth rate of $\mu_P^{max} = 5 \times 10^{-5}\mathrm{s}^{-1}$. In these simulations nutrient losses through biological growth were compensated for by a nutrient flux $\langle w\mathrm{N}^* \rangle$ into the boundary layer through the base z_S of the simulation domain. Since losses from the former are easily outweighed by gains from the latter, the effect over time is to create a nutricline, with significantly higher nutrient concentrations at the base of the layer compared to the surface. Consider the $(U_*, U_S) = (2.0, 2.2)$ case Fig. 8a first. The mixing layer of $z_{ML} \approx z_{TD}/2 = 10\mathrm{m}$ is relatively shallow, insufficient for any of the extra nutrient added at the base to be vertically mixed into the surface region. So it simply accumulates, uselessly, in the lower layers. However, this is of little import since the initial nutrient level $N = 1.0$ is already sufficient to support immediate *P* growth. However, this growth is not uniformly distributed across the boundary layer. Instead a *DBM* forms at a depth $z = 8 - 15\mathrm{m}$, at or just below the point $z_{ML} \approx z_{TD}/2$ where $\varepsilon(z) \approx 0$. The position and form of the simulated *DBM* is strikingly similar to those recorded in the experimental datasets shown in Fig.1 (which are for *DCM*). This illustrates the importance of M13's results, since most other observational reports on *DCM* do not include any corresponding measure of turbulent mixing. This numerical modelling work strongly supports M13's observations that the two are indeed correlated. Notice too that *DBM* is not brought about by the presence of the nutricline, because that has not had time to form as yet. The numerical *DBM* is a transient feature, lasting about 5 days or so because, just as in the simplified model illustrated in Fig. 6, the growth in the *P* concentration promotes a corresponding surge in the zooplankton concentration. A numerical *DZM* forms at a similar depth but somewhat after the *DBM*, consuming the latter before itself dies off. This restores the biological fields to a uniform (not the initial) state after about 20 days. One would anticipate the cycle would be repeated roughly in accordance with the dynamical properties

discussed for the simplified model (for these parameters $\tau_{oscil} \approx 12$ days at a depth of $z \approx 7$m), although this has not happened by the end of the simulation. For the $(U_*, U_S) = (3.0, 3.3)$ simulation shown in Fig. 8b, the results are broadly similar. Again the $z_{ML} \approx z_{TD}/2 = 15$m depth is still too shallow for much of the replenishment nutrient added at $z_S = 50$m to be mixed into the surface region. But with initial nutrient levels already high across the simulation domain, a *DBM* still forms relatively quickly. As before the *DBM* forms just below $z_{TD}/2$, between $z = 17 - 23$m, persists for about 5 days, before being consumed by the numerical *DZM*, which itself dies out through lack of food after about 15 days. Notice the initial *DBM* is thicker than in Fig. 8a but less intense. This fits with statistical analysis of M13 (specifically Fig. 4 of that paper) that within the $DCM_{depth} \pm 0.5DCM_{thick}$ range, the highest fluorescence values are associated with smaller values of $\varepsilon(z)$. However, for the strongest wind forcing case (Fig. 8c) the results are quite different. In this instance no *DBM* forms. Instead the *P* profile grows almost uniformly across the whole of the simulation domain, before being consumed by the growth in zooplankton it has stimulated.

It is worth looking more closely at why no *DBM* forms for the $(4.0, 4.4)$ case, when based on the other less windy simulations, one might expect a somewhat less intense maxima to occur somewhere about $z = 25$m. There are two possible reasons. First the $\varepsilon(z)$ profiles derived turbulent kinetic energy budget equation, have a tendency to underestimate the extent of the *vertical* mixing lower down in the boundary layer. This can be seen by examining the horizontally averaged vertically velocity variance profiles $\langle w^2 \rangle_T$ for the three simulation regimes (Figs. 9a-c). For the low wind case $(2.0, 2.2)$, the $\langle w^2 \rangle_T$ profile closely matches the corresponding $\varepsilon(z)$ profile (cf. Figs.7a & 9a), but for the higher wind cases the $\langle w^2 \rangle_T$ profile decays more slowly and penetrates to a deeper level than the corresponding $\varepsilon(z)$ profiles. This behaviour is also a feature of other LES ocean boundary layer codes (e.g. McWilliams *et al.* 1997, Pearson *et al.* 2015) which incorporate Langmuir circulations. It is also evident

from M13 experimental measurements of $\varepsilon(z)$ (Fig.1) that energy dissipation does not abruptly cease at one particular depth, but rather there is evidence of intermittent turbulent bursts extending below $peak_{depth} - peak_{thick}$. Polten and Belcher (2007) point out that in contrast to classic shear driven boundary layers, inclusion of significant wave effects characterised by the Stokes drift term U_S, results in increased vertical transport associated with the formation of down-welling jets carrying fluid down as far as the turbulent depth z_{TD}. This feature is probably a factor underlying the strong sub-surface peaks observed in the $\varepsilon(z)$ profiles recorded at the North Atlantic/Antarctic sites. For the strong wind/wave $(4.0, 4.4)$ simulation this enhanced vertical mixing penetrates to $z_{TD} = 40\text{m}$, preventing the formation of a *DBM* in this instance. The other possible reason is that in this instance the setting of $z_S = 50\text{m}$ is too small, and if the simulation domain were to be extended to say $z_S = 75\text{m}$ it would be large enough facilitate the generation of a weak *DBM*. M13's observations show that *DBM* can occur at depths down to 100m or so, in boundary layers subject to genuinely strong $U_* > 5.0 \times 10^{-3}\text{ms}^{-1}$ wind forcing conditions.

Figs. 10a-c show the evolution of the biological (N, P, Z) profiles for the same three boundary layers as before, only this time the replenishing nutrient flux is applied at the surface rather than the base. So unlike in the previous examples, this extra nutrient is mixed throughout the mixing layer, eventually reaching depths close to z_{TD} for the $(4.0, 4.4)$ simulation. Although a surface flux is a somewhat unrepresentative of how nutrient replenishment typically occurs within ocean mixing layers, it provides a means, within the model constraints, of making the extra nourishment readily available to the biological populations in those regions of the water column where *DBM* formed previously. For the low and intermediate wind simulations $(2.0, 2.2)$ & $(3.0, 3.3)$ the initial behaviour is much as before, with transient *DBM* forming at around $z_{ML} \approx z_{TD}/2$ (the extra surface nutrient means the *DBM* form slightly closer to the surface and are more intense). However, the main

effect of adding replenishment nutrient at the surface is to stimulate the appearance of a secondary *DBM*, about 15 days after the primary *DBM* was consumed by the zooplankton population. The secondary *DBM* develop at the same depths as the primary and last about the same time, but are slightly less intense. For the strong wind $(4.0, 4.4)$ simulation the extra vertical mixing prevents the formation of either a primary or secondary *DBM*, much as before. Two points come out of this. First, *DBM* formation is clearly a fairly robust process, which operates independently of changes in the nutrient distribution within the boundary layer. Provided enough nutrient is present initially and the mixing is not too strong, *DBM* are very likely to form. Second, if background nutrient levels remain fairly high through some effective means of replenishment as in Fig.10, there is a tendency for the characteristic biological timescales to manifest themselves over and above the homogenising tendencies of the physical boundary layer drivers. Hence the formation of the secondary *DBM*, seen in the low wind simulations, occurs after about 15 days, close to the predicted $\tau_{oscil} \approx 12$ days timescale derived from the biological parameters alone. By contrast, secondary *DBM* had not formed by the end of the base flux simulations, because not enough nutrient was present to stimulate them.

5b) Sensitivity to predation pressure and nutrient initial conditions

The simulations presented in the previous section assumed a relatively large ($r_Z = 3 \times 10^{-4}$m) zooplankton predator, with a correspondingly large contact radius $R = 1.2 \times 10^{-2}$m and swimming capabilities $\sigma_Z = 2 \times 10^{-4}\mathrm{ms}^{-1}$. It is interesting to investigate what happens if the predator were made somewhat smaller, reduced in size to $r_Z = 5 \times 10^{-5}$m, with the other parameters rescaled accordingly (see Table 2, e.g. $\sigma_Z = 5 \times 10^{-5}\mathrm{ms}^{-1}$ and $R = 2 \times 10^{-3}$m). The effect of these basic size reductions is to dramatically slow down the predation rate for an individual predator. This is illustrated in Fig. 11, which shows the corresponding predation rate calculated from a $\varepsilon(z)$ profile taken from a $(U_*, U_S) = (3.0, 3.3)$ simulation

(with $z_S = -33\text{m}$ rather than $z_S = -50\text{m}$). Compared to the corresponding profile for the large predator (Fig. 7b), the individual capture cross section has fallen by a factor of ~200. However, smaller predators tend to be more numerous than larger ones. In these illustrative examples the background concentration for the large predator was set to 10^2 cells m^{-3}, increasing to 2×10^4 cells $\text{m}^{-3}$for the smaller predator. This effectively offsets the drop in capture cross section, meaning the *overall* predation pressure on the *P* field is little changed.

Fig. 12 shows the evolution of the biological (N, P, Z) profiles based upon the small zooplankton predator with replenishment nutrient added at the base. Compared to the corresponding evolution profiles $(U_*, U_S) = (3.0, 3.3)$ for the large predator, shown in Fig. 8b, a couple of distinctive features are obvious. On this occasion the initial *DBM* forms at just below $z = z_{TD}/2$ between about 15-20m much as before, but then two secondary *DBM* evolve, after about 10 and 20 days respectively. The reason for this much faster evolution lies in the fact that the death rate of the small predator has increased by a factor of $10/3$ compared to that of the large predator (smaller organisms tend to have shorter life-spans). From the analysis of Section 4 this reduces $\tau_{oscil} = 2\pi/\sqrt{a\mu_{Z\,death}}$ to about 6.5 days, leading to the production of two secondary *DBM* over the T_{sim} interval. The other distinctive feature is that the secondary *DBM* are almost as intense as the primary and form a little deeper in the water column. This can be put down to the fact that the simulation domain is somewhat shallower than previously, which means that it is easier for nutrient added at the base to reach the regions where *DBM* formation occurs. So it is more easily accessible for the phytoplankton, producing a strong response in the secondary growth phases. Looking at the corresponding results for a surface nutrient flux in Fig. 13 (cf. Fig. 10b for the large predator) the results are broadly similar to the base flux results, with the formation of two secondary *DBM*, although on this occasion they are slightly less intense than the primary. Since nutrient entering at the surface is mixed more thoroughly throughout the mixing layer, the background

concentration never reaches the levels seen in the base flux results, reducing the intensity of the secondary growth surge. Notice too that the mixing has the effect of gradually merging the secondary maxima together, so the *DBM* becomes a more permanent feature of the boundary layer. Overall, these results show that phytoplankton populations residing in the turbulent boundary layer will tend to evolve to form *DBM* a little below $z_{TD}/2$, provided the boundary layer contains enough nutrient to stimulate them. These *DBM* are robust features of the biological dynamics, and form independently of the finer details of the predation pressures imposed by different zooplankton species. So observations of *DBM* formation in real biophysical boundary layers, which may contain a myriad of co-existing/competing planktonic species, should not be surprising.

These conclusions lead to the question what would happen if the initial nutrient conditions were not conducive to *DBM* formation? To this end a simulation was carried out with $(N, P, Z)_{t=0} = (0.1, 0.5, 0.5)$, to see what effect a very small initial nutrient concentration would have on the development of the biological fields. In this simulation the wind forcing was relatively low $(U_*, U_S) = (2.5, 2.8)$, and nutrient replenishment was added through the surface. The phytoplankton field was subject to a predation pressure term similar to that shown in Fig. 11, except that in this case the swimming contribution was switched off $\sigma_Z = 0.0\mathrm{ms}^{-1}$. This was compensated for by a reduction in the reaction time to $T_R = 1\mathrm{s}$. Since the predator can no longer swim, it means that the phytoplankton field is not actually subject to any predation pressure below the turbulent depth $z_{TD} \approx 25\mathrm{m}$, because in this region there are neither advective nor swimming motions to bring a predator/prey pair into close proximity. The corresponding (N, P, Z) profiles are shown in Fig. 14. The outstanding feature of these results is the formation not of a *DBM*, but instead a near *uniform* biological profile extending across nearly all the turbulent depth. But the circumstances of the evolution of this feature are significant. Since $N_{t=0} = 0.1$ is so low, the initial behaviour of both the (P, Z) fields is to die

off through lack of food resources. As the boundary layer is replenished with nutrient (notice it never quite reaches the starting value of $N = 1.0$ for the previous simulations) the phytoplankton is able to respond with renewed growth after about 15 days. However, at this time the zooplankton population *is still virtually extinct,* so there is no predation pressure to retard the phytoplankton growth in the upper regions of the mixing layer. Consequently the growth is close to uniform across the mixing layer and no significant *DBM* forms. The decline in the phytoplankton growth rate due to reductions in the ambient light level across the mixing layer is insufficient, in itself, to generate a *DBM*. (There is some variation due to the light. After 18 days, when the global concentration of P reaches a maximum, $\langle P \rangle = 1.78$ at the surface, increasing to $\langle P \rangle = 2.06$ at $z = -0.65 z_{TD}$, a difference of 14%. But this is small amount compared to the 50−300% differences seen in the experimental results of Fig. 1 and the simulations in which predation pressure is significant.) Instead the strength of the vertical mixing ensures that all the different P cells are exposed to roughly the same amount light, and consequently they all grow at the roughly the same rate. After 20 days or so the zooplankton population starts to recover in response to the new food resource now available. It too grows uniformly across the boundary layer. One would anticipate that if the simulation were to be run for a longer period of time, then on the next population cycle a situation more akin to the previous simulations would pertain and *DBM* formation would occur. This is because the nutrient conditions would no longer be so extreme as to force both planktonic fields to near extinction and hence the higher predation pressure near the surface would again manifest itself. It also suggests that the observational *DBM* recorded by M13 formed as they did because a) their boundary layers were either well stocked, or recently replenished, with significant amounts of nutrient and b) the low fluorescence measurements found in the surface regions are a consequence of high predation pressure in those localities. To investigate these points further, Fig. 15 shows what happens in the scenario when the

predation term is switched off altogether. Starting from a standard, nutrient rich $(N, P, Z)_{t=0} = (1.0, 0.5, 0.5)$ initial profile, the zooplankton population starves and quickly dies out. Unrestrained by predation, the phytoplankton population grows rapidly to very high concentrations, almost uniformly across those parts of the boundary layer where there is sufficient nutrient to support the excess growth (in the top layers for the surface flux, Fig. 15a; at or below z_{TD} for the base flux, Fig. 15b). Again there is little sign that the decline in the ambient light level with depth is a sufficient stimulus (by itself) to initiate significant *DBM* formation in these wind driven boundary layers.

A variation on this theme is to initiate a simulation with a non-uniform $N_{t=0}$ profile. Two such examples are shown in Fig. 16. Fig. 16a shows a run beginning with a moderately high $N = 1.4$ nutrient concentration near the surface, declining uniformly to a minimum value of $N = 0.2$ at $z = z_S$. The subsequent behaviour of the (N, P, Z) profiles from this initial state is interesting. Near the surface the abundance of nutrient promotes rapid growth in the phytoplankton population, but this in turn is rapidly consumed by the zooplankton. Since the reaction time $T_R = 1\text{s}$ of this small predator is rapid, it is able to feed very efficiently near the surface. Consequently the phytoplankton population has hardly any time to establish itself before it is consumed and hence the P concentration falls away. One can infer its transient presence by the small predator characteristic $\tau_{oscil} \approx 6.5$ day period still to be seen in the upper zooplankton profiles. Lower down one sees the formation of a very intense DBM at a depth of about 20m, somewhat deeper than those shown in Figs. 8, 10 & 12. Formation at this depth is brought about by the juxtaposition of the relatively high nutrient levels from the initial profile, remaining in situ due to the lack of mixing, in combination with a rapid decline in predation pressure to near zero, again caused by the lack of any mixing or swimming to bring about predator/prey contacts. This *DBM* also lasts longer than those generated in other simulations and is not subject to the $\tau_{oscil} \approx 6.5$ day period which pertains in the upper layers

where strong predation pressure is a factor. The initially imposed nutricline in effect creates two somewhat disconnected boundary layers, in which the biological dynamics evolves at different rates. Fig. 16b shows what happens if the initial nutrient profile is inverted from high-low to low-high. As in Fig.15b, the low level of predation at depths $z < z_{TD}$ combined with easily availability of nutrients (as distinct from Fig. 16a), initially produces very high phytoplankton concentrations. But in this scenario, unlike in Fig. 15b, there is sufficient predation pressure to regulate this growth after just a few days. Higher up (and somewhat overshadowed by the growth near z_S) a *DBM* again develops around 20m as in Fig. 16a. The higher ambient nutrient concentration in this case means it is actually twice as intense (cf. the contrasting P concentration scales in Fig. 16) as the *DBM* which develops from the high-low nutricline.

The intensity scales of both DBM shown in Fig. 16 would indicate that they are somewhat artificial constructs (none of the observed *DBM* recorded by M13 show such a high level of intensity), brought about by an extremely favourable correlation between the initial nutrient profiles and the rapid decline in both mixing and predation levels below $z_{TD}/2$. Nevertheless, they serve to highlight the hypothesis that those regions of the water column which are most favourable to *DBM* formation are those that exhibit a), sufficiently high nutrient and light levels to promote growth in combination with b), a significant fall off in the ambient predation pressure. Since sharp reductions in $\varepsilon(z)$ bring about a corresponding easing in predation pressure at or just below $z_{ML} \approx z_{TD}/2$, it is not surprising that simulated *DBM* are seen to develop around this depth. It would also explain the strong observational correlations, manifest in M13's datasets, between the location of real *DBM* and those regions of the water column where the energy dissipation rate is in decline (Fig. 1).

5c) Horizontal Distribution

Since the LES-NPZ model carries out three dimensional simulations, it is worth trying to discern any significant patterns in the evolution of the biological fields when viewed across a horizontal plane. Periodically during the course of each simulation, instantaneous snapshots of the horizontal distribution of the biological fields are recorded at various different depths. These can then be processed to create 'movies' of the biological fields as they evolve during a simulation (copies of these 'movies' are available from the authors on request). Some examples of these snapshots, taken from the $(U_*, U_S) = (3.0, 3.3)$ surface nutrient flux simulation (q.v. Fig. 10b for the corresponding vertical profiles), are shown Figs 17-19. Fig. 17 is taken at a depth of 10m after 4.7 days, whilst Figs. 18 & 19 are for a depth of 20.4m after 4.7 and 5.9 days respectively. The significance of these latter two selections is that they represent samples taken from the primary *DBM*, which from Fig. 10b is seen to reach its maximum intensity at ~20m after around four days. But first it is interesting to consider why the *DBM* does not form at a shallower depth, at say 10m for example. Fig.17 shows the instantaneous vertical velocity field w at the same moment as the corresponding biological correlations. The w field exhibits the characteristic Langmuir turbulence pattern of up and down-welling zones (McWilliams *et al.* 1997, Lewis 2005, Polten & Belcher 2007, Teixeira & Belcher 2010), in this case rotated clockwise (~40^0) from the wind direction (the x-axis) by a combination of the Coriolis forcing and the Stokes drift term (see Lewis & Belcher 2004). This 'streakiness' pattern of elongated up and down-welling zones is replicated (but to a lesser extent) in the biological fields. It is particularly noticeable in the distribution of the P field, which exhibits a correlation between high phytoplankton concentrations and vertical down-welling. Since nutrient is being added at the surface in this instance, the down-welling regions act, in effect, as richer local food environs for the phytoplankton, providing the spur they need for significant extra growth (~up to 7% more than the horizontal mean concentration). Notice that this all happens relatively quickly, because the N field shows a

significant absence of nutrient in the down-welling zones, presumably because the excess has already been utilised to boost the growth of the local phytoplankton population. Assuming an average down-welling velocity of $w \approx 2 \times 10^{-3}\mathrm{ms}^{-1}$ around this depth, it would take about 500s for any excess nutrient to be advected a distance of 1m. This would be time enough to produce differentials in the P concentration field of between ~1-2% (assuming a light reduced P growth rate of $\sim 3.3 \times 10^{-5}\mathrm{s}^{-1}$), roughly what is observed. The much slower growing zooplankton ($\mu_Z^{max} = 2.9 \times 10^{-6}\mathrm{s}^{-1}$) are not sensitive enough to respond to stimuli over as (relatively) short a time period as 500s, and hence the distribution of the Z field is almost completely uniform in the horizontal (cf. the small colour-scale changes in Fig. 17d).

Looking at the corresponding horizontal distributions recorded at the exact same point in time, but at a depth of 20m (Fig. 18), one is immediately struck by the fact that the vertical mixing is somewhat weaker and the 'streakiness' pattern of elongated up and down-welling zones is less pronounced. As a result those regions of the P field distribution exhibiting higher than average growth (shown in yellow), now cover a broader area than in Fig. 17. What seems to be happening is that by the time one reaches a depth of $z \approx 20\mathrm{m}$, the excess nutrient is no longer being confined to the strictly defined down-welling zones that transported it from the surface. This idea is supported by the velocity variance data shown in Fig. 3a (from a simulation with comparable wind forcing) which shows that at $z \approx 10\mathrm{m}$ the vertical $\langle w^2 \rangle_T$ velocity component is dominant, but by $z \approx 20\mathrm{m}$ the horizontal combination of $\langle u''^2 \rangle_T + \langle v''^2 \rangle_T$ exceeds that of $\langle w^2 \rangle_T$. This would produce a pooling effect, caused by the replenishment nutrient spreading out (horizontally) from the disintegrating down-welling zones. This pooling of nutrient, *in combination with* the reduced zooplankton predation pressure at this depth, then promotes the formation of the primary *DBM* in this region. Notice that the pooling of nutrient is not directly apparent from the N-field itself because on arrival it would be quickly absorbed by the phytoplankton based on the timescales mentioned above.

Rather it manifests itself in the relatively uniform excess growth seen in the P field distribution. In future it would be interesting to test this pooling hypothesis quantitatively, by carrying out simulations to monitor the average horizontal flux of nutrients at different depths to see if *DBM* formation corresponds to increased levels of horizontal mixing. Fig. 19 shows values of the biological fields at this depth after about 6 days, just as the primary *DBM* is starting to break down. Over the interval of 1.3 days between Figs. 18 & 19, the zooplankton has had the opportunity to generate excess growth in response to the increased higher P field concentrations, increasing the local predation pressure, which ultimately destroys the *DBM* feature.

6. Conclusions

The study of the formation and the underlying factors that drive DCM/DBM formation has a long history (Cullen 2015 and reference therein). The literature would seem pretty much exhaustive. However, the recent publication by M13 of various open ocean datasets which unequivocally link *DCM* formation and levels of background turbulent mixing (something previously that has only been speculated on), provides a new slant and calls for a more detailed investigation of this phenomena. Advances in computing power and resources allow one, using the LES methodology, to simulate three dimensional, wind and wave driven turbulent boundary layers in great detail. By coupling such simulations to a generic type of NPZ model specially adapted to reflect the influence of background turbulence levels on growth and predation rates, one has the means to carry out just such an investigation.

The results reported here largely corroborate the findings of M13. Provided the wind forcing is not too strong (q.v. Figs. 8c & 10c) and the boundary layer is relatively nutrient rich, the simulations predict *DCM/DBM* formation at depths at or just below half the

turbulent depth $\approx z_{TD}/2$, the level at which the upper mixing layer starts to peter out, very similar to the observational data. This depth is a robust feature, as the *DCM/DBM* continue to form here irrespective of whether the nutrient profile is uniform (primary *DBM*), or develops in the presence of a nutricline (either bottom up or top down) as seen in the secondary *DBM* (Figs. 10a-b,12, 13 & 16). The simulations also support the idea that *DCM/DBM* are generated primarily in response to predation pressure (Figs. 14-16). Starting the simulations from a very low nutrient base (see Fig. 14) effectively switches off the predation pressure by starving the zooplankton population to near extinction. In its absence, when phytoplankton growth was re-initiated by replenishment of nutrient through the surface, growth resumed uniformly and no *DBM* formed. Removing the predation term altogether from the model, also inhibited *DBM* formation (Fig.15). Taken together, these results indicate that whilst the vertical mixing is sufficiently vigorous to circulate phytoplankton cells throughout the upper mixing layer so that they all get to experience pretty much the same amount of light, it is not vigorous enough to offset the retardation in growth experienced near the surface through increased levels of predation pressure (see the various predation rate profiles). This is not too surprising because increases in turbulent mixing generate corresponding increases in predation pressure (provided the predator can react fast enough to capture the extra prey contacts it makes), but has relatively little influence on the amount of light penetrating the mixing layer. It is also significant that the *DBM* formed irrespective of the type of predator (large or small) was used. This conclusion concerning the importance of predation pressure in *DCM/DBM* formation was also reached by Fennel & Boss (2003) in their (somewhat simpler) mathematical modelling work. It is just possible that *DCM/DBM* formation could be initiated by *a combination* of retarded light level growth and a strong positive nutricline (low nutrient at the surface, high at the base) without the need for any predation pressure (this hypothesis is not specifically tested here). However given the results shown in Fig. 14, such a combination

of stimuli does not seem sufficient to produce the intense *DBM* observed in Fig. 1. Rather this work tends to support the ideas expressed by Banse (2013) of the importance of "top-down" processes in *DCM/DBM* formation, since phytoplankton growth is usually matched or exceeded by grazing losses.

The question as to why the *DBM* form at the depth they do is intriguing. From the investigations here, the depth $z_{TD}/2$ marks the point at which the coherence of the Langmuir cells driven by the wind and wave generated turbulence starts to break down. The vertical velocity component, which up that point is the dominant feature of the boundary layer turbulence, weakens (see Fig. 3a) and the horizontal components become more prevalent. This leads to a rapid increase in the vertical nutrient gradient as $\langle w^2 \rangle_T$ declines (see Fig. 10), and a smoothing out of the horizontal gradients as the relative strength $\langle u''^2 \rangle_T + \langle v''^2 \rangle_T$ increases (cf. Figs. 16 & 17). In combination this would tend to lead to a pooling of nutrient at around this depth, initiating a strong phytoplankton growth in response. If so, this work indicates that *DCM/DBM* formation can actually be influenced by the surface wave characteristics driving the Langmuir turbulence regime. A surprising connection, given that in the past it has been assumed that surface wave effects were simply too small to significantly influence even the ocean boundary layer dynamics, let alone the associated biology.

This effect could also be brought about by other features of the flow, such as the presence of shallow thermo/pycnocline acting to restrict the extent of the vertical transport. Since the boundary layers generated in these simulations are unstratified, it is difficult to definitively rule this out. However, in their observations M13 found that the position of the DCM_{depth} lay some ~18m (on average) below the corresponding $\varepsilon(z)\ peak_{depth}$ when stratification was relatively low (Section 2). This strongly suggests that their *DCM* were not brought about by

the presence of a pycnocline. Indeed Fennel and Boss (2003) argue that in contrast to relatively small lakes (e.g. Simmonds *et al.* 2015), the density changes associated with shallow pycnoclines found in *the open ocean* would be too small to disrupt vertical transport very significantly. This idea is supported by the experimental $\varepsilon(z)$ profiles of M13 (Fig. 1) and the numerical vertical velocity profiles shown in Fig. 9, which both show that vertical mixing does not shut off abruptly at around $z_{TD}/2$ but continues to exert an influence to a least twice this depth. This would tend to disrupt and deepen pycnoclinic formation, making it unlikely this is the cause of M13's observed *DCM*.

The *DCM/DBM* generated in these simulations are transient, lasting no more than a few days. However, this is due to the fact that the biological $P - Z$ fields are two generic representations of many different planktonic species. In reality *DCM/DBM* found in the ocean will contain many different species each subject to their own specific growth and predation cycles. So in the absence of any very strong mixing events, observed *DCM* are likely to be longer lasting than those generated here, although their species composition may change over time. This idea could be tested in more detail by introducing more separate biological species (e.g. by having the large predator feeding directly on the small predator which in turns feeds on the *P* field) into the simulations, provided suitable biological coupling terms could be introduced into the model equations (3-5). Future developments of this kind should enable better parameterizations for the simpler, but very much faster 1D biophysical models most commonly in use. And if experimental development is such that the recording of physical measurements (e.g. more $\varepsilon(z)$ sampling) in conjunction with biological ones becomes the norm, then there is scope to develop specialised LES-NPZ models in order to study very specific planktonic ecosystems.

References

Baird, M. E., & S. M. Emsley. 1999. Towards a mechanistic model of plankton population dynamics. J. Plankton Res. 21, 85-126.

Baird, M. E., S. M. Emsley, & J. M. McGlade. 2001. Modelling the interacting effects of nutrient uptake, light capture and temperature on phytoplankton growth. J Plankton Res. 23, 829-840.

Banse, K. 2013. Reflections about chance in my career, and on the top-down regulated world. Anu. Rev. Mar. Sci. 5, 1-19.

Bees, M. A., I. Mezic, & J. M. McGlade. 1998. Planktonic interactions and chaotic advection in Langmuir circulations. Math. Comput. Simul. 44, 527-544.

Benoit-Bird, K. J., T. J. Cowles, & C. E. Wingard. 2009. Edge gradients provide evidence of ecological interactions in planktonic thin layers. Limnol. and Oceanogr. 54 (4), 1382-1392.

Coleman, G., J. Ferziger, & P. Spalart. 1990. A numerical study of the turbulent Ekman layer. J. Fluid Mech. 213, 313-348.

Craik, A.D.D. & S. Leibovich. 1976. A rational model for Langmuir circulations. J. Fluid Mech. 73, 401-426.

Cullen, J.J. 1982. The deep chlorophyll maximum: comparing vertical profiles of chlorophyll a. Can. J. Fish. Aqua. Sci. 39, 791-803.

Cullen, J.J., 2015. Subsurface chlorophyll maximum layers: enduring enigma or mystery solved? Ann. Rev. Mar. Sci. 7, 207-239.

de Boyer Montégut, C., G. Madec, A. S. Fischer, A. Lazar, & D. Iudicone. 2004. Mixed layer depth over the global ocean: An examination of profile data and a profile-based climatology. J. Geophys. Res. Oceans 109, C12003, 1-20.

Dekshenieks, M.M., P. L. Donaghay, J. M. Sullivan, J. E. B. Rines, T. R. Osborn, & M. S. Twardowski. 2001. Temporal and spatial occurrence of thin phytoplankton layers in relation to physical processes. Mar. Ecol. Prog. Ser. 223, 61-71.

Denman, K. L., & A. E. Gargett. 1995. Biological-physical interactions in the upper ocean: the role of vertical and small-scale transport processes. Ann. Rev. Fluid Mech. 73, 401-426.

Denman, K. L., & M. L. Peňa. 1999. A coupled 1-D biological/physical model of the northeast subarctic Pacific Ocean with iron limitation. Deep-Sea Res. II 46, 2877-2908.

Doubell, M. J., H. Yamazaki, H. Li, & Y. Kokuby. 2009. An advanced laser based fluorescence microstructure profiler (TurboMAP-L) for measuring bio-physical coupling in aquatic systems. J. Plankton Res. 31, 1441-1452.

Durham, W. M., J. O. Kessler, & R. Stocker. 2009. Disruption of vertical motility by shear triggers the formation of thin planktonic layers. Science 323 1067-1070.

Edwards, A. M., & J. Brindley. 1996. Oscillatory behaviour in a three-component planktonic population model. Dyn. Stabil. Syst. 11, 347-370.

Edwards, C. A., T. A. Powell, & H. P. Batchelder. 2000. The stability of an *NPZ* model subject to realistic levels of vertical mixing. J. Mar. Res. 58, 37-60.

Estrada, M., C. Marrasé, M. Latasa, F. Berdalet, M. Delgado, & T. Riera. 1993. Variability of deep chlorophyll maximum characteristics in the Northwestern Mediterranean. Mar. Ecol. Prog. Ser. 92, 289-300.

Fasham, M. J. R., H. W. Ducklow, & S. M. McKelvie. 1990. A nitrogen-based model of plankton dynamics in the oceanic mixed layer. J. Mar. Res. 48, 591-639.

Fennel, K., & E. Boss. 2003. Subsurface maxima of phytoplankton and chlorophyll: Steady-state solutions from a simple model. Limnol. Oceanogr. 48, 1521-1534.

Flierl, G., & D. J. McGillicuddy. 2002. Mesoscale and submesoscale physical-biological interactions. In: Robinson, A. R., McCarthy, J. J. Rothschild, B. J. (Eds.) The Sea, vol. 12 Wiley, New York, pp. 113-185.

Frogner, P., Gíslason, S. R. & N. Óskarsson. 2001. Fertilizing potential of volcanic ash in ocean surface water. Geology 29.6, 487-490,

Franks, P. J. S. 1995. Coupled physical-biological models in oceanography. Rev. Geophys. (Suppl. July) 1177-1187.

Franks, P. J. S. 2002. NPZ models of plankton dynamics: their construction, coupling to physics and application. J. Oceanogr. 58, 379-387.

Galbraith, P. S., H. I. Browman, R. G. Racca, A. B. Skiftesvik, & J. F. Saint-Pierre. 2004. The effect of turbulence on the energetic of foraging in Atlantic cod (*Gadus morhua*) larvae. Mar. Ecol. Prog. Ser. 281, 241-257.

Garratt, J. 1992. The Atmospheric Boundary Layer (Appendix 3). Cambridge University Press.

Gregg, A. C. 1989. Scaling turbulent dissipation in the thermocline. J. Geophys. Res. 94 9686-9698.

Hamilton, D. P., K. R. O'Brien, M. A. Burford, & J. D. Brookes. 2010 Vertical distributions of chlorophyll in deep, warm monomictic lakes. Aquatic Sciences-Research Across Boundaries 72, 295-307.

Hansen, P. J., P. K. Bjornsen, & B. W. Hansen. 1997. Zooplankton grazing and growth: scaling within the 2-2000 micro m body size range. Limnol. Oceanogr. 42, 697-704.

Hoecker-Martinez, M. S., & W. D. Smyth. 2012. Trapping of gyrotatic organisms in an unstable shear-layer. Continental Shelf Res. 36, 8-18.

Holm-Hansen, O., M. Kahru & C. D. Hewes 2005. Deep chlorophyll *a* maxima in pelagic Antarctic waters. II. Relation to bathymetric features and dissolved iron concentrations. Mar. Ecol. Prog. Ser. 297, 71-81.

Huisman, J., N.N. Pham Thi, D. M. Karl & B. Sommeijer 2006. Reducing mixing generates oscillations and chaos in the oceanic deep chlorophyll maximum. Nature 439, 322-325.

Johnston, T. M. S., O. M. Cheriton, J. T. Pennington, & F. P. Chavez. 2009. Thin phytoplankton layer formation at eddies, filaments, and fronts in a coastal upwelling zone. Deep-Sea Research II 56 246-259.

Lesieur, M. 1997. Turbulence in Fluids (3rd edition). Kluwer Academic Publishers, Netherlands.

Letelier, R. M., D. M. Karl, M. R. Abbott, & R. R. Bidigare. 2004. Light driven seasonal patterns of chlorophyll and nitrate in the lower euphotic zone of the North Pacific Subtropical Gyre. Limnol. Oceanogr. 49, 508-519.

Lewis, D. M., & T. J. Pedley. 2001. The influence of turbulence on plankton predation strategies. J. Theor. Biol. 210 347-365.

Lewis, D. M., 2003. Planktonic encounter rates in homogeneous isotropic turbulence: the case of predators with limited fields of sensory perception. J. Theor. Biol. 222, 73-97.

Lewis, D. M., 2005. A simple model of plankton population dynamics coupled with a LES of the surface mixed layer. J. Theor. Biol. 235, 565-591.

Lewis, D. M., & S. I. Bala. 2006. Plankton predation rates in turbulence: A study of the limitations imposed on a predator with a non-spherical field of sensory perception. J. Theor. Biol. 242, 44-61.

Lewis, D. M. & S. I. Bala. 2008. An examination of salutatory predation strategies employed by fish larvae foraging in a variety of different turbulent regimes. Mar. Ecol. Prog. Ser. 359, 261-274.

Lewis, D. M., & S. E. Belcher. 2004. Time-dependent, coupled, Ekman boundary layer solutions incorporating Stokes drift. Dyn. Atmos. Oceans 37 313-351.

Lewis, D. M., & T. J. Pedley. 2001. The influence of turbulence on plankton predation strategies. J. Theor. Biol. 210, 347-365.

Longhurst, A., & A. Harrison. 1989. The biological pump, profiles of plankton production and consumption in the upper ocean. Prog. in Oceanogr. 22, 47-123.

Macías, D., L. M. Lubian, F. Echevarría, E. Huertas, & C. M. García. 2008. Chlorophyll maxima and mass interfaces: tidally induced dynamics in the Strait of Gibraltar. Deep-Sea Res. I 55, 832-846.

Macías, D., A. Rodríguez-Santana, E. Ramírez-Romero, M. Bruno, J. L. Pelegrí, P. Sangrà, B. Aguiar-Gonzàlez, & C. M. García. 2013. Turbulence as a driver for vertical plankton distribution in the subsurface upper ocean. Scientia Mar. 77, 541-549. (abbreviated as M13).

MacKenzie, B. R. & W. C. Leggett. 1995. Encounter rates and swimming behaviour of pause-travel and cruise larval fish predators in calm and turbulent laboratory environments. Limnol. Oceanogr. 40, 1278-1289.

McManus, M. A., plus 24 co-authors, 2003. Characteristics, distribution and persistence of thin layers over a 48 hour period. Mar. Ecol. Prog. Ser. 261, 1-19.

McManus, M. A., O. M. Cheriton, P. J. Drake, D. V. Holliday, C. D. Storlazzi, P. L. Donaghay, & C. F. Greenlaw. 2005. Effects of physical processes on structure and transport of thin zooplankton layers in the coastal ocean. Mar. Ecol. Prog. Ser. 301, 199-215.

McWilliams, J. C., P. P. Sullivan, & C. H. Moeng. 1997. Langmuir turbulence in the ocean. 334, 1-30.

McComb, W. D. 1991. The Physics of Fluid Turbulence. Oxford University Press, Oxford, UK.

Moum, J. N. & T. R. Osborn 1986. Mixing in the main thermocline. J. Phys. Oceanogr. 16, 1250-1259.

Muelbert, J. H., M. R. Lewis, & D. E. Kelley. 1994. The importance of small-scale turbulence in the feeding of herring larvae. J. Plankton Res. 16, 927-944.

Pearson, B. C., A. L. M. Grant, J. A. Polten, & S. E. Belcher. 2015. Langmuir turbulence and surface heating in the ocean surface boundary layer. J. Phys. Oceanogr. 45, 2897-2911.

Pérez, V., E. Fernández, E. Marañón, X. A. G. Morán, & M. V. Zubkov. 2006. Vertical distribution of phytoplankton biomass, production and growth in the Atlantic subtropical gyres. Deep-Sea Res. I, 53, 1616-1634.

Philips, O.M. 1977. The Dynamics of the Upper Ocean. Cambridge University Press, Cambridge, UK.

Polten, J. A., & S. E. Belcher. 2007. Langmuir turbulence and deeply penetrating jets in an unstratified mixed layer. J. Geophys. Res. 112, C09020, doi:10.1029/2007/JC004205.

Polten, J. A., D. M. Lewis, & S. E. Belcher. 2005. The role of wave-induced Coriolis-Stokes forcing on the wind driven mixed layer. J. Phys. Oceanogr. 35, 444-457.

Rothschild, B. J., & T. R. Osborn. 1988. Small-scale turbulence and planning contact rates. J. Plankton Res. 12 1152-1162.

Ruiz, J., D. Macías, & F. Peters. 2004. Turbulence increases the average settling velocity of phytoplankton cells. Proc. Natl. Acad. Sci. USA 101, 17720-17724.

Simmonds, B., S. A. Wood, D. Őzkundakci, & D. P. Hamilton. 2015. Phytoplankton succession and the formation of a deep chlorophyll maximum in a hypertrophic volcanic lake. Hydrobio. 745, 297-312.

Smagorinsky, J. 1963. General circulation experiments with the primitive equations, I: the basic experiment. Mon. Weather Rev. 91, 99-164.

Straile, D. 1997. Gross growth efficiencies of protozoan and metazoan zooplankton and their dependence on food concentration, predator-prey ratio and taxonomic group. Limnol. Oceanogr. 42, 1375-1385.

Sullivan, P. P., J. C. McWilliams, & C. H. Moeng. 1994. A subgrid-scale model for large-eddy simulation of planetary boundary layer flows. Bound.–Layer Met. 71, 247-276.

Teixeria, M. A. C., & S. E. Belcher. 2002. On the distortion of turbulence by a progressive surface wave, J. Fluid Mech. 458, 229-267.

Tennekes, H., & J. Lumley. 1972. A First Course in Turbulence. MIT Press, Cambridge, MA USA.

Wang, Z., & L. Goodman. 2010. The evolution of a thin phytoplankton layer in strong turbulence. Cont. Shelf Res. 30, 104-118.

White, B., & K. Matsumoto. 2012. Causal mechanisms of the deep chlorophyll maximum in Lake Superior: A numerical modelling investigation. 38 504-513.

Williams, R. G., & M. J. Follows. 1998. The Ekman transfer of nutrients and maintenance of new production over the North Atlantic. Deep-Sea Res. I 45, 461-489.

Acknowledgments

The authors would like to acknowledge the technical help of S. Downing (University of Liverpool) with certain computational aspects of this work and R. Bearon (University of Liverpool) for proof reading the manuscript and useful comments. J. T. Siddons was supported by a 2013 EPSRC Doctoral Training Award: reference EP/L505018/1. The authors would also like to thank two anonymous reviewers for their helpful insights and suggestions concerning this work.

Figure Captions

Figure 1. Four illustrative fluorescence (left) and energy dissipation rate profiles taken from Fig. S1 of the paper by Macías *et al.* 2013, showing how *DCM* are to be found just below $z = peak_{depth}$, where $\langle \varepsilon(z) \rangle$ reaches its maximum value ε_{max}. The measurements are taken from four different sites. Profile 6 is from the Alboran Sea; Profile 21 is from the Strait of Gibraltar; Profile 28 is near the Antarctic peninsula; Profile 31 is from the North Atlantic. Full details of these sites, along with many further similar profiles are presented in Macías *et al.* 2013.

Figure 2. Time (over a period $T = T_{sim}$) and spatially averaged velocity profiles $\langle u \rangle_T$ —— and $\langle v \rangle_T$ $- - -$ (units ms^{-1}). Data derived from a $(U_*, U_S) = (3.5, 3.9)$ simulation.

Figure 3. a) Time (over a period $T = T_{sim}$) and spatially averaged velocity variance profiles $\langle u''^2 \rangle_T$ —— , $\langle v''^2 \rangle_T$ ····· and $\langle w^2 \rangle_T$ $- - -$, normalised by U_*^2. Data derived from the $(U_*, U_S) = (3.5, 3.9)$ simulation. b) Evolution of $\langle u''^2 \rangle_T$, over periods of $T =$ $5, 8, 12, 16$ & 19 days. Data derived from the $(U_*, U_S) = (5.0, 5.6)$ simulation.

Figure 4. Time (over a period $T \approx 1$ day) and spatially averaged kinetic energy dissipation rate profiles $\varepsilon(z)$. Data derived from the $(U_*, U_S) = (2.0, 2.2)$ —— , $(3.5, 3.9)$····· and $(5.0, 5.6)$ $- - -$ simulations.

Figure 5. Illustrative profiles of the variation of the predation rate integral $I(R, T_R, \varepsilon, 0)$ for a non-swimming predator and contact radius $R = 2 \times 10^{-3}$m. Data derived from the $(U_*, U_S) = (2.0, 2.2)$ —— , $(3.5, 3.9)$····· and $(5.0, 5.6)$ $- - -$ simulations with 5a) $T_R = 5$s and 5b) $T_R = 15$s.

Figure 6. Evolution of the mean concentrations of Nutrient, Phytoplankton & Zooplankton derived from the simplified NPZ model for $\mu_P^{max} = 2.5 \times 10^{-5}\mathrm{s}^{-1}$ with other biological parameters as in Table 2.

Figure 7. Energy dissipation profiles (left) and the corresponding zooplankton predation rate profiles (right) taken from three LES-NPZ model simulations subject to a) low wind $(U_*, U_S) = (2.0, 2.2)$, b) intermediate wind $(U_*, U_S) = (3.0, 3.3)$ & c) high wind $(U_*, U_S) = (4.0, 4.4)$ forcing. The predation profiles are based upon data for the large predator (Table 2) with $\sigma_Z = 2 \times 10^{-4}\mathrm{ms}^{-1}$, $T_R = 5\mathrm{s}$ and $R = 1.2 \times 10^{-2}\mathrm{m}$.

Figure 8. Evolution profiles of the normalised $\langle N \rangle, \langle P \rangle$ & $\langle Z \rangle$ concentrations, starting from initial values of $(1.0, 0.5, 0.5)$ respectively. An inward nutrient flux boundary condition is implemented at the *base* $z_s = -50\mathrm{m}$ of the simulation domain. a) low wind $(U_*, U_S) = (2.0, 2.2)$, b) intermediate wind $(U_*, U_S) = (3.0, 3.3)$ & c) high wind $(U_*, U_S) = (4.0, 4.4)$ forcing. Biological data as given in Table 2, incorporating the large zooplankton predator.

Figure 9. Evolution of the (normalised) vertical velocity variance $\langle w^2 \rangle_T$ profile recorded during different stages of a typical set of simulations. a) low wind $(U_*, U_S) = (2.0, 2.2)$, b) intermediate wind $(U_*, U_S) = (3.0, 3.3)$ & c) high wind $(U_*, U_S) = (4.0, 4.4)$ forcing. Note the greater penetration depths compared to the corresponding energy dissipation profiles shown in Fig. 7.

Figure 10. Evolution profiles of the normalised $\langle N \rangle, \langle P \rangle$ & $\langle Z \rangle$ concentrations, starting from initial values of $(1.0, 0.5, 0.5)$ respectively. An inward nutrient flux boundary condition is implemented at the *surface* $z_s = 0\mathrm{m}$ of the boundary layer. a) low wind $(U_*, U_S) = (2.0, 2.2)$, b) intermediate wind $(U_*, U_S) = (3.0, 3.3)$ & c) high wind $(U_*, U_S) = (4.0, 4.4)$ forcing. Biological data as given in Table 2, incorporating the large zooplankton predator.

Figure 11. Energy dissipation profile (left) and the corresponding zooplankton predation rate profile (right) taken from the intermediate wind $(U_*, U_S) = (3.0, 3.3)$ forced simulation. The predation profiles are based upon data for the small predator (Table 2) with $\sigma_Z = 5 \times 10^{-5}\mathrm{ms}^{-1}$, $T_R = 5\mathrm{s}$ and $R = 2 \times 10^{-3}\mathrm{m}$.

Figure 12. Evolution profiles of the normalised $\langle N \rangle, \langle P \rangle$ & $\langle Z \rangle$ concentrations, starting from initial values of $(1.0, 0.5, 0.5)$ respectively for intermediate wind $(U_*, U_S) = (3.0, 3.3)$ forcing. An inward nutrient flux boundary condition is implemented at the base $z_s = -33\mathrm{m}$ of the simulation domain. Biological data as given in Table 2, incorporating the small zooplankton predator.

Figure 13. Evolution profiles of the normalised $\langle N \rangle, \langle P \rangle$ & $\langle Z \rangle$ concentrations, starting from initial values of $(1.0, 0.5, 0.5)$ respectively for an intermediate wind $(U_*, U_S) = (3.0, 3.3)$ forcing. An inward nutrient flux boundary condition is implemented at the *surface* $z_s = 0\mathrm{m}$ of the boundary layer. Biological data as given in Table 2, incorporating the small zooplankton predator.

Figure 14. Evolution profiles of the normalised $\langle N \rangle, \langle P \rangle$ & $\langle Z \rangle$ concentrations, starting from initial values of $(0.1, 0.5, 0.5)$ respectively for an intermediate wind $(U_*, U_S) = (2.5, 2.8)$ forcing. An inward nutrient flux boundary condition is implemented at the *surface* $z_s = 0\mathrm{m}$ of the boundary layer. Biological data as given in Table 2, incorporating the small zooplankton predator, except here it is non-swimming $\sigma_Z = 0.0\mathrm{ms}^{-1}$ and fast reacting $T_R = 1\mathrm{s}$.

Figure 15. Evolution profiles of the normalised $\langle N \rangle, \langle P \rangle$ & $\langle Z \rangle$ concentrations, starting from initial values of $(1.0, 0.5, 0.5)$ respectively, for an intermediate wind $(U_*, U_S) = (2.5, 2.8)$ forcing. In this instance the zooplankton predation term is *switched off*. Fig. 15a is for a

surface nutrient flux; whilst in 15b it is imposed at the base of the simulation domain. Other data as in Fig. 14.

Figure 16. Evolution profiles of the normalised $\langle N \rangle, \langle P \rangle$ & $\langle Z \rangle$ concentrations for an intermediate wind $(U_*, U_S) = (2.5, 2.8)$ forcing. In Fig. 16a, the initial nutrient profile forms a nutricline, ranging from $0.2 - 1.4$ for $z = -33$ to $z = 0$m respectively. In Fig. 16b, this initial profile is inverted, with low concentration at the surface and high at the base. Other data as in Fig. 14.

Figure 17. Instantaneous contour plots of the horizontal $(x\text{-}y)$ distribution of a) the vertical velocity field $w(\boldsymbol{x}, t)$ $\{= w''(\boldsymbol{x}, t)$, since $\langle w \rangle = 0\}$, b) nitrate, c) phytoplankton, d) zooplankton and at a depth of $z = 10$m. The data was recorded 4.7 days into the intermediate wind $(U_*, U_S) = (3.0, 3.3)$ simulation, just at the point when the primary DBM is reaching its maximum extent (see Fig. 10b for the corresponding vertical profiles). Here the sampling depth lies somewhat above the *DBM* level.

Figure 18. Instantaneous contour plots of the horizontal $(x\text{-}y)$ distribution of a) the vertical velocity field $w(\boldsymbol{x}, t)$, b) nitrate, c) phytoplankton, d) zooplankton and at a depth of $z = 20.4$m. The data was recorded 4.7 days into the intermediate wind $(U_*, U_S) = (3.0, 3.3)$ simulation, just at the point when the primary DBM is reaching its maximum extent (see Fig. 10b for the corresponding vertical profiles). Here the sampling depth corresponds to the centre of the *DBM* .

Figure 19. Key as Fig. 18, except on this occasion the data was recorded after 5.9 days. At this time the primary *DBM* is coming to an end of its lifespan, as raised levels of zooplankton predation signal its destruction.

Tables

Parameter and Symbol	Numerical Value
Acceleration due to gravity g	$9.81\mathrm{ms}^{-2}$
Coriolis Frequency f	$10^{-4}\mathrm{s}^{-1}$
Density of Water ρ_0	$1000\mathrm{kgm}^{-3}$
Viscosity of water μ	$1\times10^{-3}\mathrm{kgm}^{-1}\mathrm{s}^{-1}$
Reference Temperature θ_r	$288.15\mathrm{K}$
Wavenumber k	$0.105\mathrm{m}^{-1}$
Stokes Drift velocity U_S	$2.2\text{-}5.6\times10^{-2}\mathrm{ms}^{-1}$
Friction Velocity U_*	$1.5\text{-}5.0\times10^{-3}\mathrm{ms}^{-1}$
Wave frequency σ	$1.015\mathrm{s}^{-1}$
Thermal expansion coefficient α†	$2\times10^{-4}\mathrm{K}^{-1}$
Buoyancy flux at $z=z_{ML}$, $\overline{w'\theta'}$	$-1.2\times10^{-6}\mathrm{Kms}^{-1}$
Monin-Obukhov length L_{MO}‡	-3.5 to $-132.7\mathrm{m}$

† In the LES, the temperature field is computed directly and the density via $\rho=\rho_0(1-\alpha\theta)$.

‡ Here $L_{MO}=U_*^3/\left(\mathrm{k}g\alpha\overline{w'\theta'}\right)$ where k ≈ 0.4 is von Kármán's constant.

Table 1. Key physical parameters used to prescribe the LES turbulent boundary layers.

Parameter and Symbol	Numerical Value
Background Z Concentration Z_0	2×10^4 (1×10^2) cells m^{-3}
Background P Concentration P_0	5×10^6 cells m^{-3}
[a]Background N Concentration N_0	2.8×10^{-5} kg m^{-3}
Z cell radius r_Z	$5 \times 10^{-5}(3 \times 10^{-4})$ m $\equiv V_Z = 5.2 \times 10^{-13}$ (1.1×10^{-10}) m^3
P cell radius r_P	$1 \times 10^{-5}\mathrm{m} \equiv V_P = 4.2 \times 10^{-15}\mathrm{m}^3$
P cell density ρ_P	$1.002\rho_0$
Z cell density ρ_Z	$1.02\rho_0$
[b]P maximum growth rate μ_P^{max}	$5 \times 10^{-5}\mathrm{s}^{-1}$
[b]Z maximum growth rate μ_Z^{max}	1.0×10^{-5} (2.9×10^{-6}) s^{-1} $\sim 2.4 \times 10^{-8} V_Z^{-0.21}$
Z death rate $\mu_{Z\,death}$	4×10^{-6} (1.2×10^{-6}) s^{-1}
Z swimming or pursuit speed σ_Z	5×10^{-5} (2×10^{-4}) ms^{-1} †
[c] Contact radius R	2×10^{-3} (1.2×10^{-2}) m †
Z reaction time T_R	1 or 5 † s
[d]Predation rate integral $I(R, T_R, \sigma_Z)$ ‡	7×10^{-10} $\mathrm{m}^3\mathrm{s}^{-1}$
[b]Yield Y	0.003 $(1.2 \times 10^{-5}) \sim 0.33\, V_P/V_Z$
[e]P growth efficiency β_E	0.75
[a]Light attenuation coefficient α	$0.04\mathrm{m}^{-1}$
$U_{sink} = 2gr_{Z/P}(\rho_{Z/P} - \rho_0)/9\mu$	$2.2 \times 10^{-3}(1.3 \times 10^{-2})$ & $4.4 \times 10^{-5}\mathrm{ms}^{-1}$
Proportion of dead P cells ϕ_P^{dead}	10^{-3}
Proportion of dead Z cells ϕ_Z^{dead}	10^{-5}
[f]Nitrate stoichiometry coefficient s_N	$2.7 \times 10^{-14}\mathrm{kgcell}^{-1} \sim 1.38 \times 10^3 V_P/3$

† Default value unless stated otherwise in text or figures.

‡ For the simple NPZ model of (20-21) *only*. For the full LES-NPZ model this is derived as a function of depth from the appropriate ε, R and T_R values, e.g. the profiles shown in Figs. 5, 7 & 11.

Table 2. Key biological parameters used to prescribe the NPZ plankton model. The zooplankton values are for the small predator, the corresponding values in parentheses are for the large predator.

Sources a) Fasham et al., 1990, b) Hansen et al., 1997, c) Muelbert et al., 1994, d) Lewis & Pedley 2001, Lewis 2005, e) Baird & Emsley 1999, f) Straile 1997.

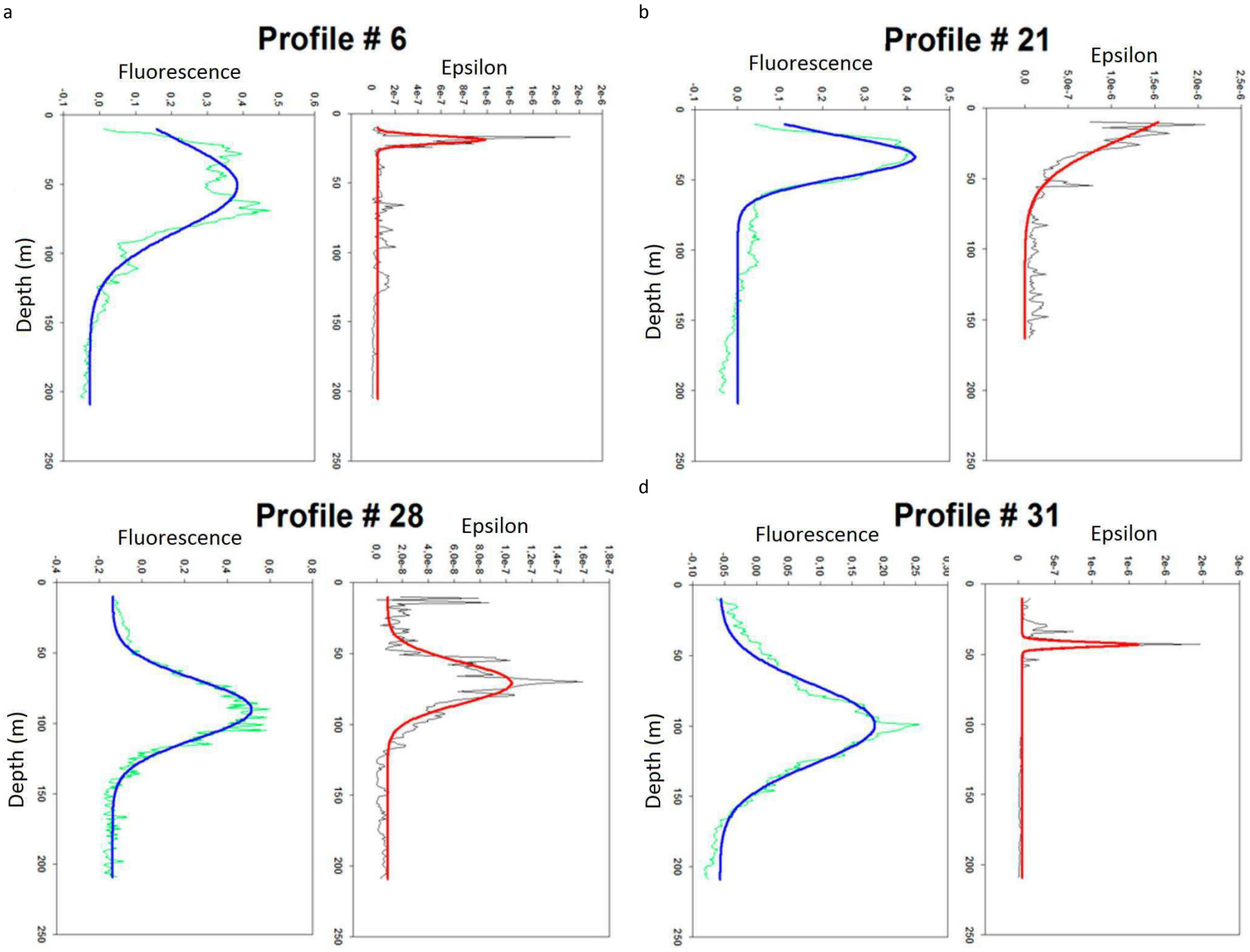
a
Profile # 6
Fluorescence
Epsilon
Depth (m)
b
Profile # 21
Fluorescence
Epsilon
Depth (m)
d
Profile # 28
Fluorescence
Epsilon
Depth (m)
Profile # 31
Fluorescence
Epsilon
Depth (m)

Figure 1

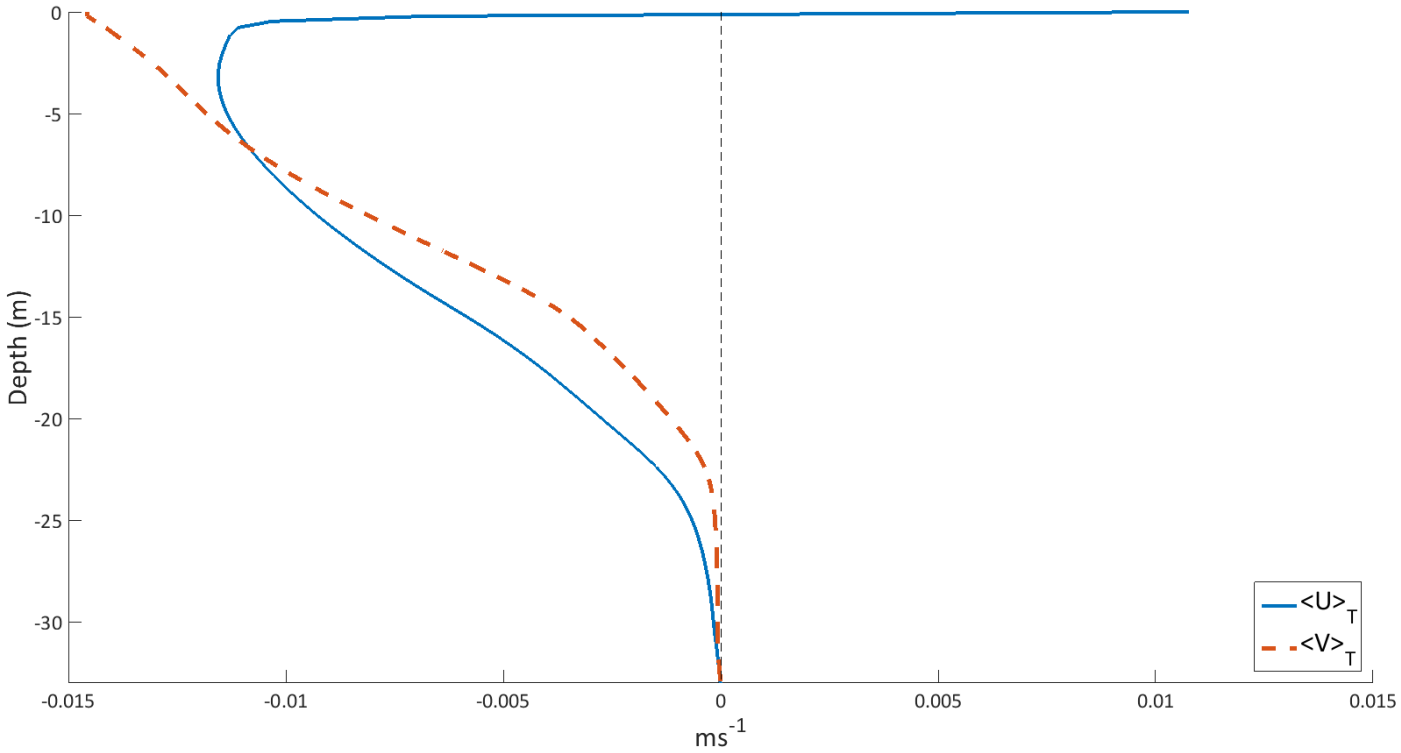

Figure 2

a

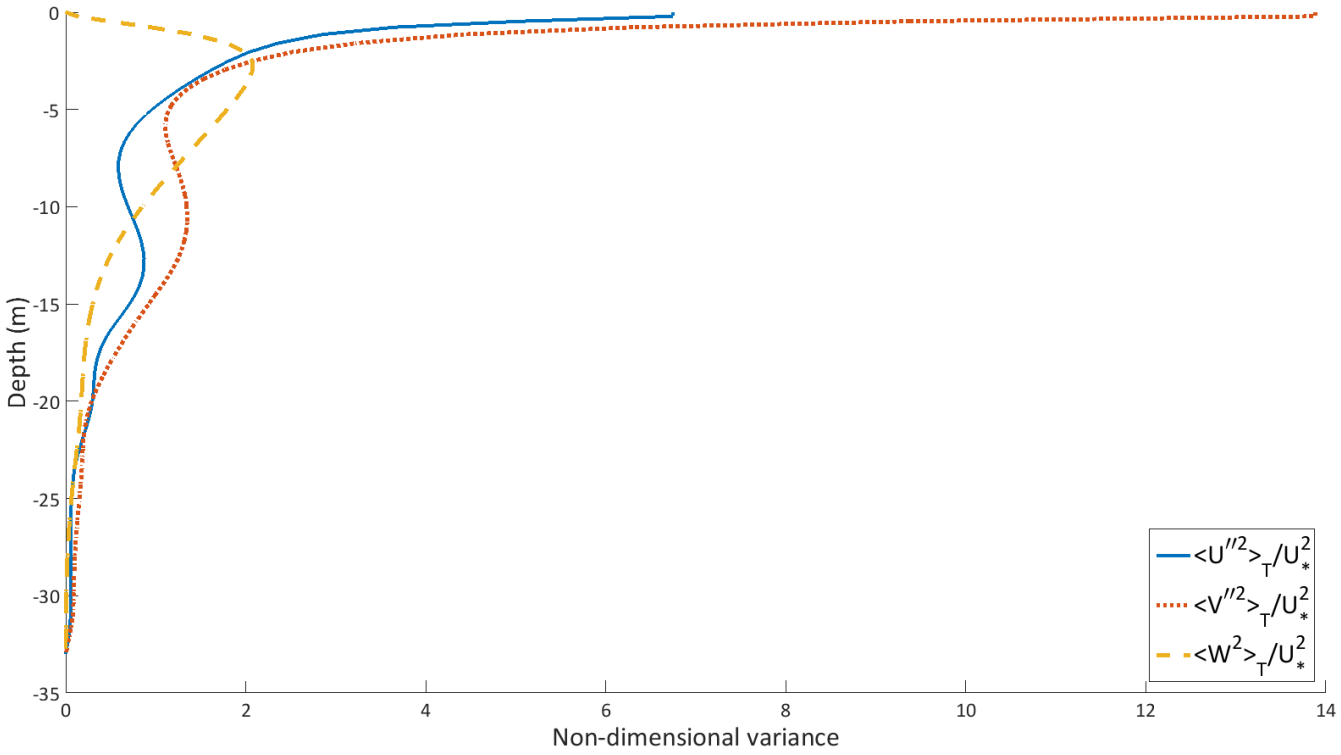
Depth (m)
Non-dimensional variance
<U''2>T/U*2
<V''2>T/U*2
<W2>T/U*2

b

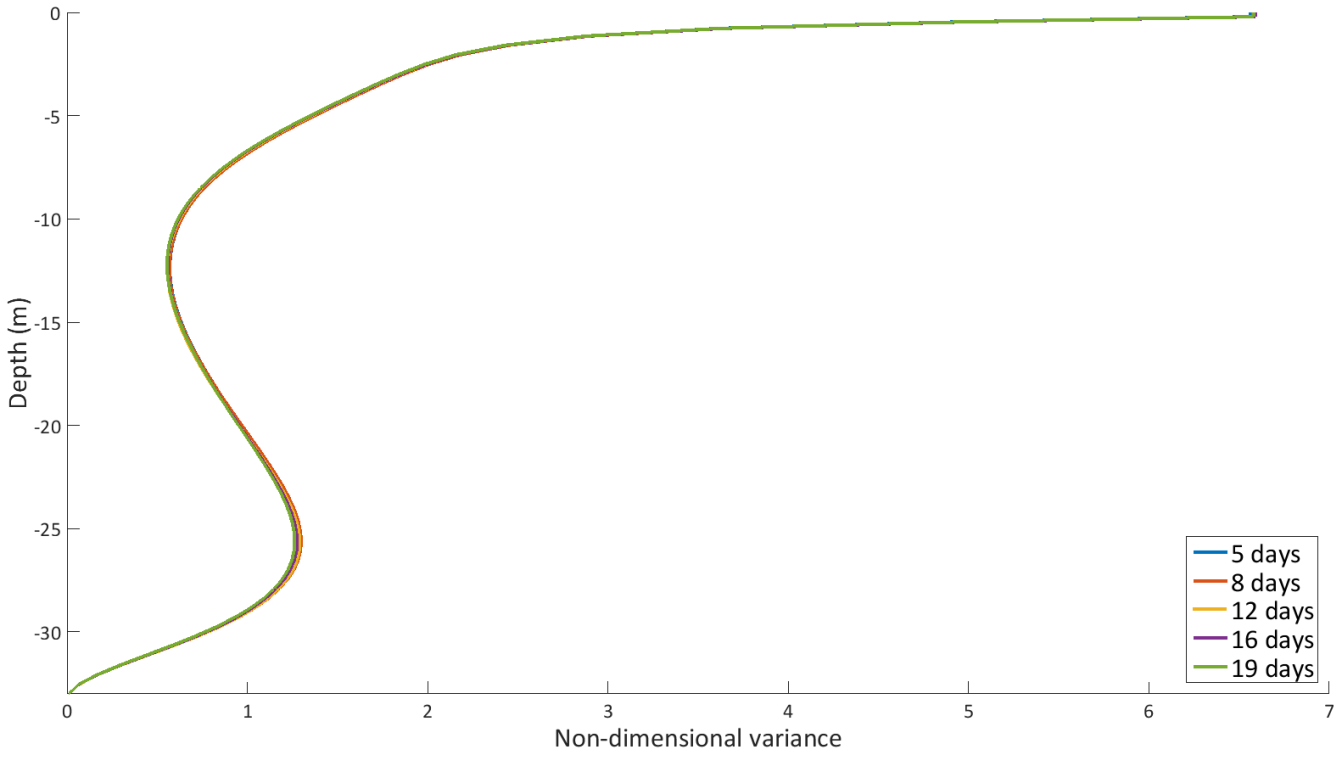
Depth (m)
Non-dimensional variance
5 days
8 days
12 days
16 days
19 days

Figure 3

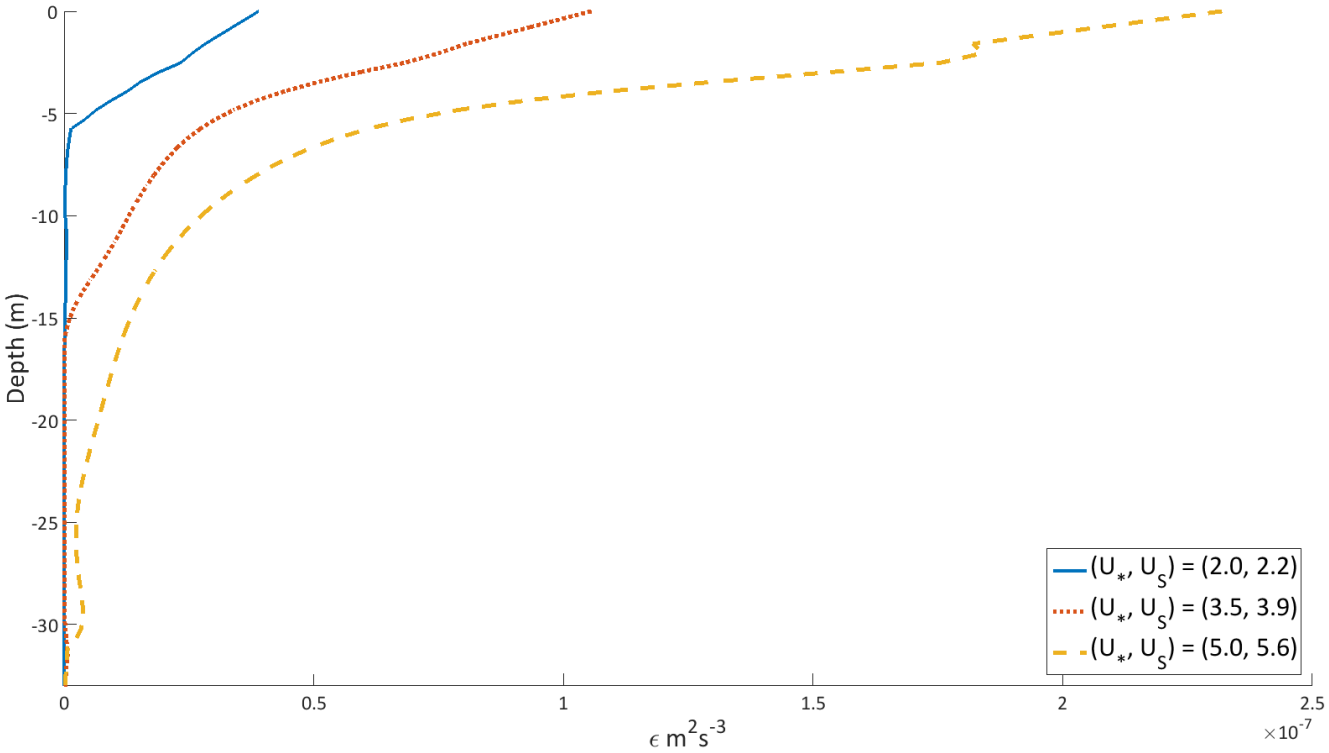
0
-5
-10
-15
-20
-25
-30
Depth (m)
0
0.5
1
1.5
2
2.5
ϵ m^{2}s^{-3}
$\times 10^{-7}$
$(U_*, U_S) = (2.0, 2.2)$
$(U_*, U_S) = (3.5, 3.9)$
$(U_*, U_S) = (5.0, 5.6)$

Figure 4

a

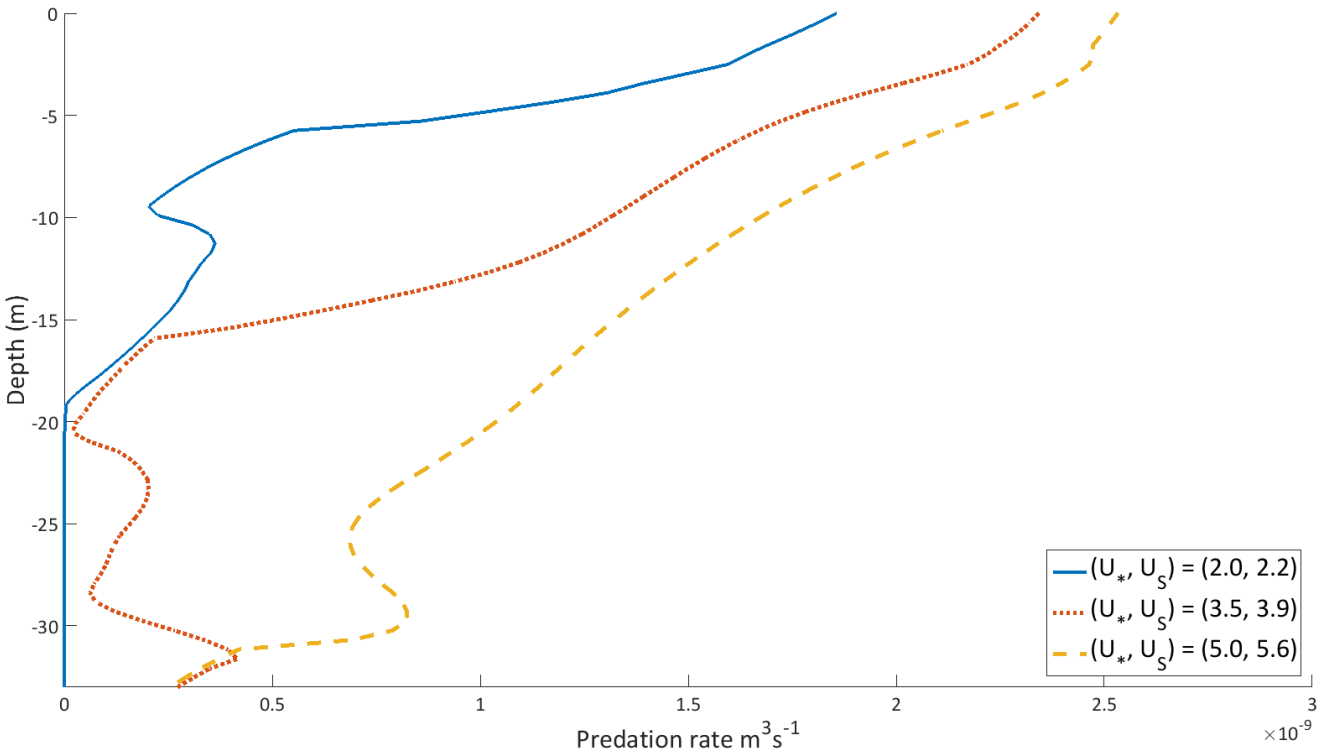
0
-5
-10
-15
-20
-25
-30
Depth (m)
0
0.5
1
1.5
2
2.5
3
Predation rate m3s-1
×10-9
(U*, US) = (2.0, 2.2)
(U*, US) = (3.5, 3.9)
(U*, US) = (5.0, 5.6)

b

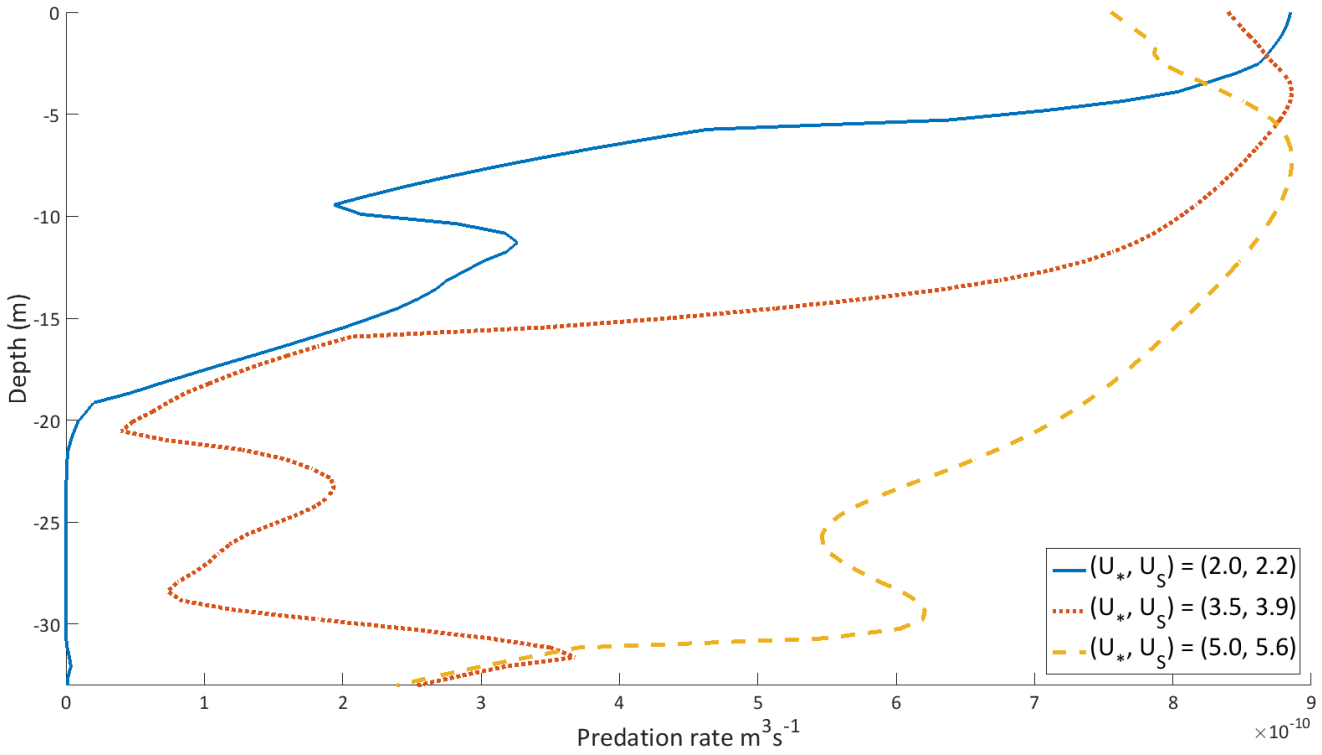
0
-5
-10
-15
-20
-25
-30
Depth (m)
0
1
2
3
4
5
6
7
8
9
Predation rate m3s-1
×10-10
(U*, US) = (2.0, 2.2)
(U*, US) = (3.5, 3.9)
(U*, US) = (5.0, 5.6)

Figure 5

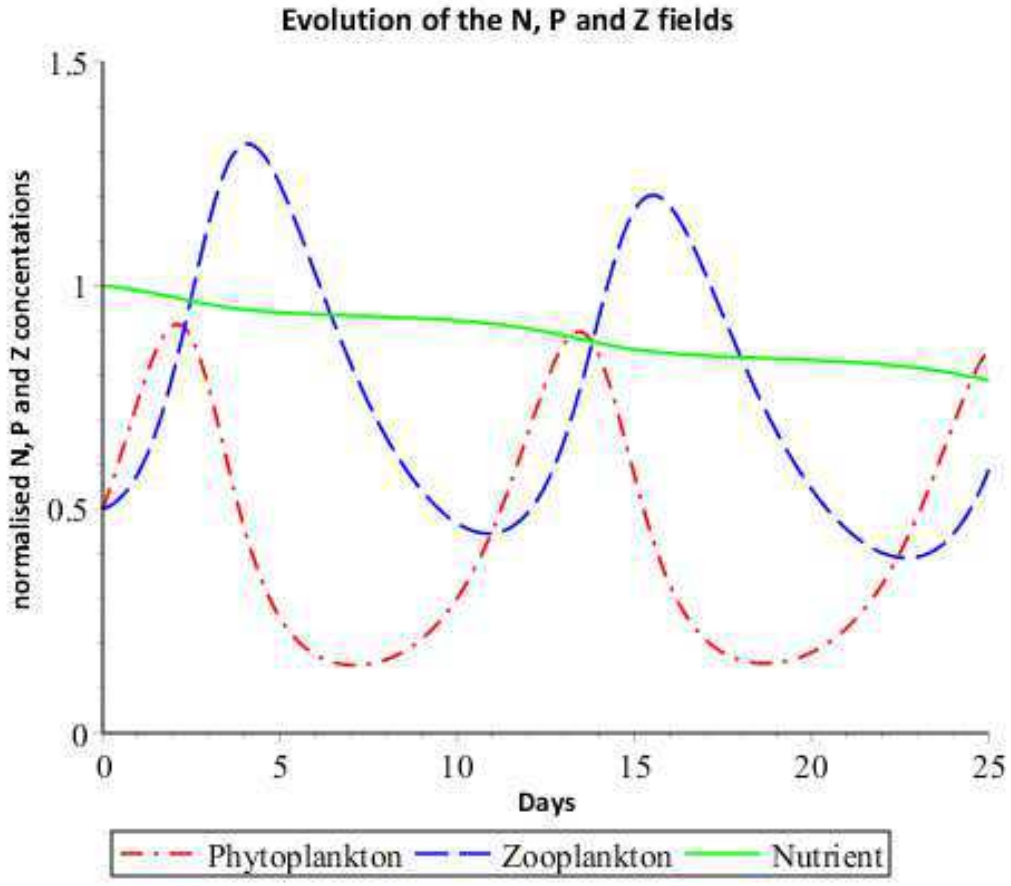
Evolution of the N, P and Z fields
normalised N, P and Z concentations
1.5
1
0.5
0
0
5
10
15
20
25
Days
Phytoplankton
Zooplankton
Nutrient

Figure 6

a

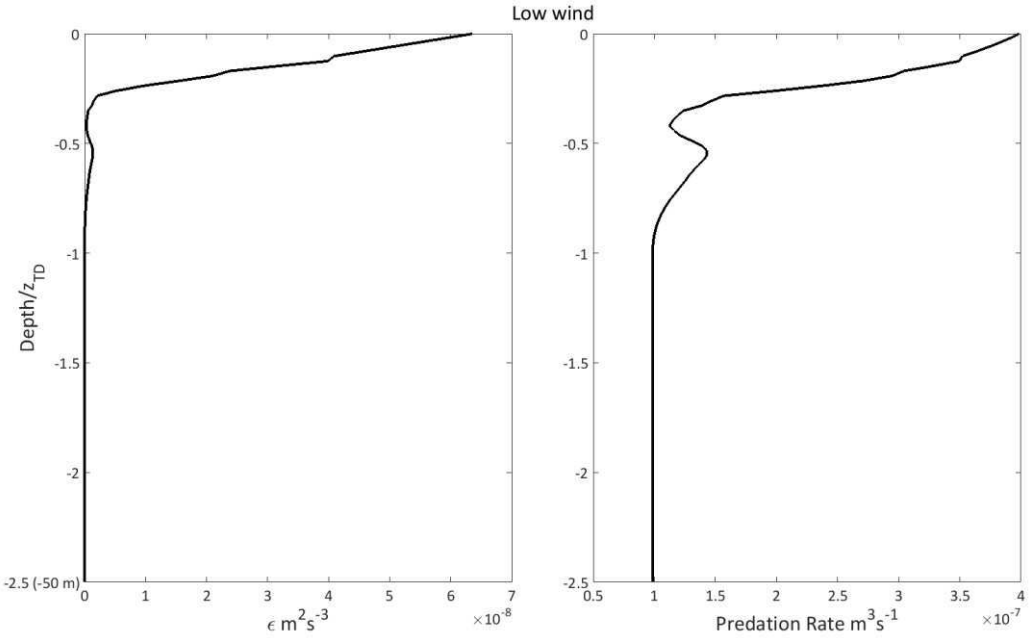
Low wind
Depth/z_{TD}
0
-0.5
-1
-1.5
-2
-2.5 (-50 m)
0 1 2 3 4 5 6 7
ϵ m^2s^{-3}
$\times 10^{-8}$
0.5 1 1.5 2 2.5 3 3.5 4
Predation Rate m^3s^{-1}
$\times 10^{-7}$

b

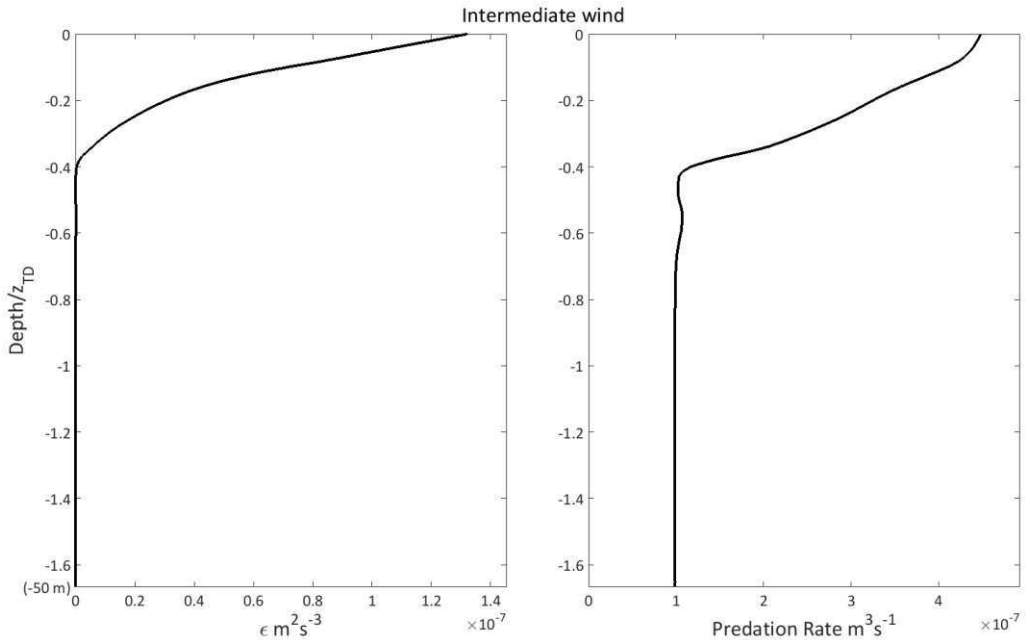
Intermediate wind
Depth/z_{TD}
0
-0.2
-0.4
-0.6
-0.8
-1
-1.2
-1.4
-1.6
(-50 m)
0 0.2 0.4 0.6 0.8 1 1.2 1.4
ϵ m^2s^{-3}
$\times 10^{-7}$
0 1 2 3 4
Predation Rate m^3s^{-1}
$\times 10^{-7}$

c

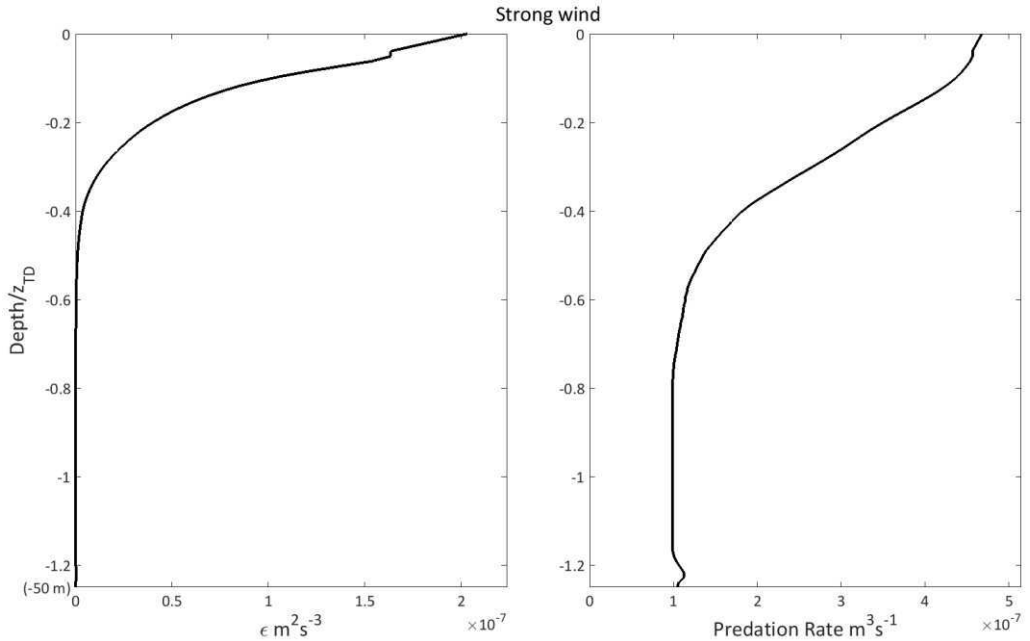
Strong wind
Depth/z_{TD}
0
-0.2
-0.4
-0.6
-0.8
-1
-1.2
(-50 m)
0 0.5 1 1.5 2
ϵ m^2s^{-3}
$\times 10^{-7}$
0 1 2 3 4 5
Predation Rate m^3s^{-1}
$\times 10^{-7}$

Figure 7

a

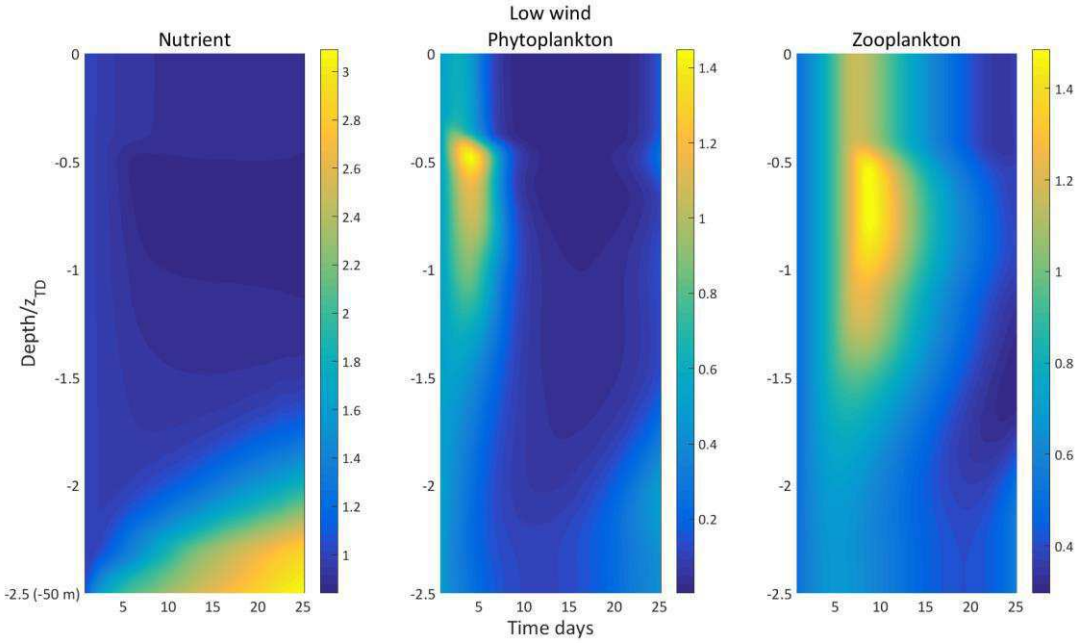
Low wind
Nutrient
Phytoplankton
Zooplankton
Depth/z_{TD}
Time days

b

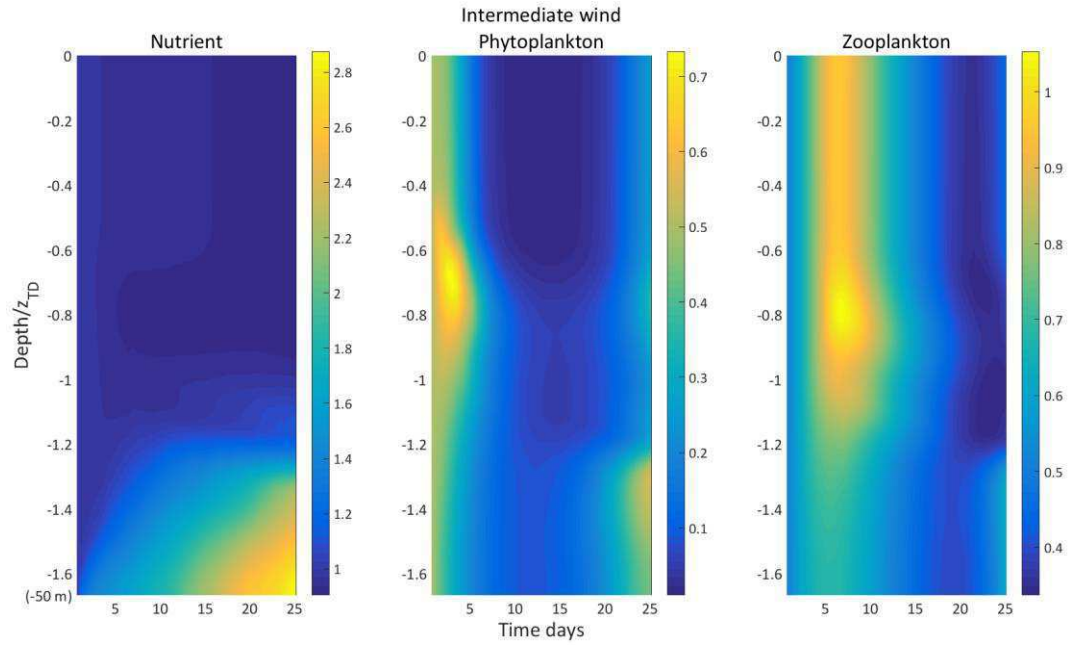
Intermediate wind
Nutrient
Phytoplankton
Zooplankton
Depth/z_{TD}
Time days

c

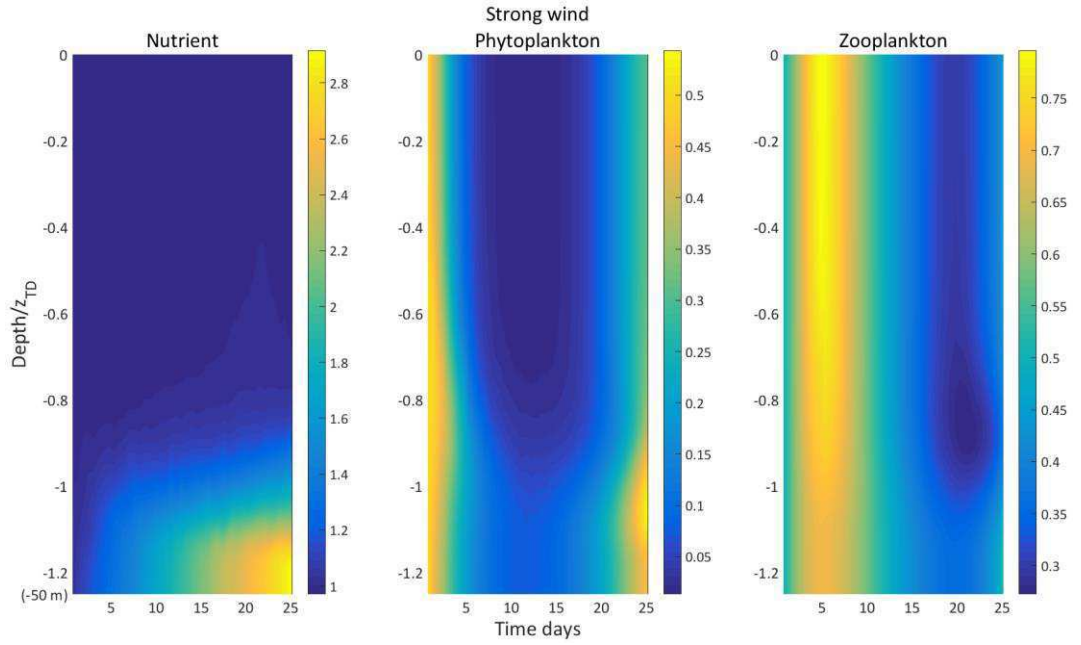
Strong wind
Nutrient
Phytoplankton
Zooplankton
Depth/z_{TD}
Time days

Figure 8

a

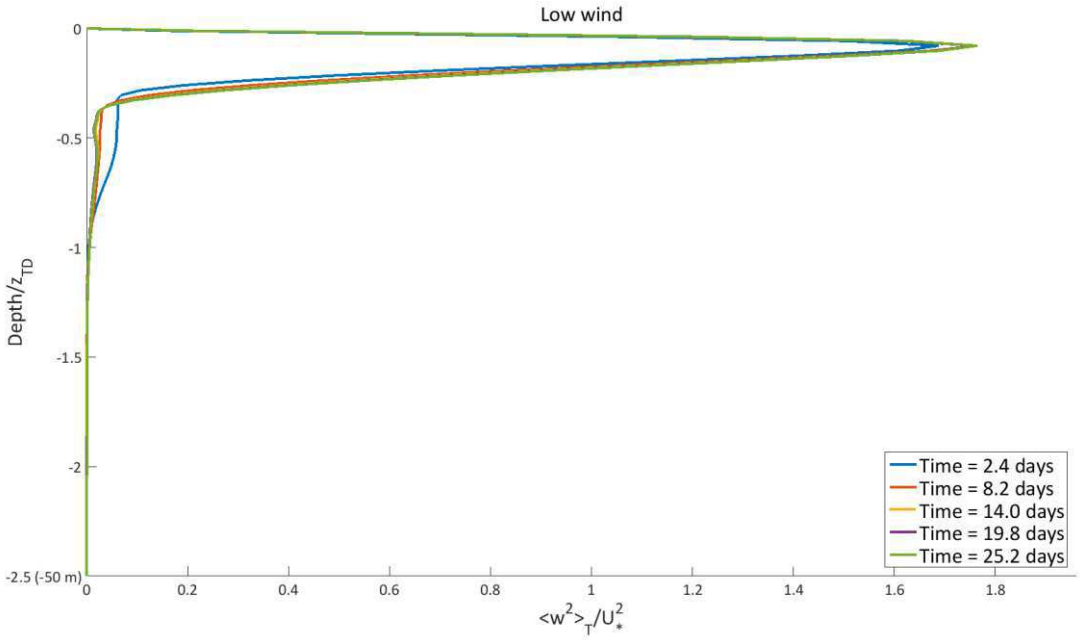
Low wind
Depth/z_{TD}
$\langle w^2 \rangle_T / U_*^2$
Time = 2.4 days
Time = 8.2 days
Time = 14.0 days
Time = 19.8 days
Time = 25.2 days

b

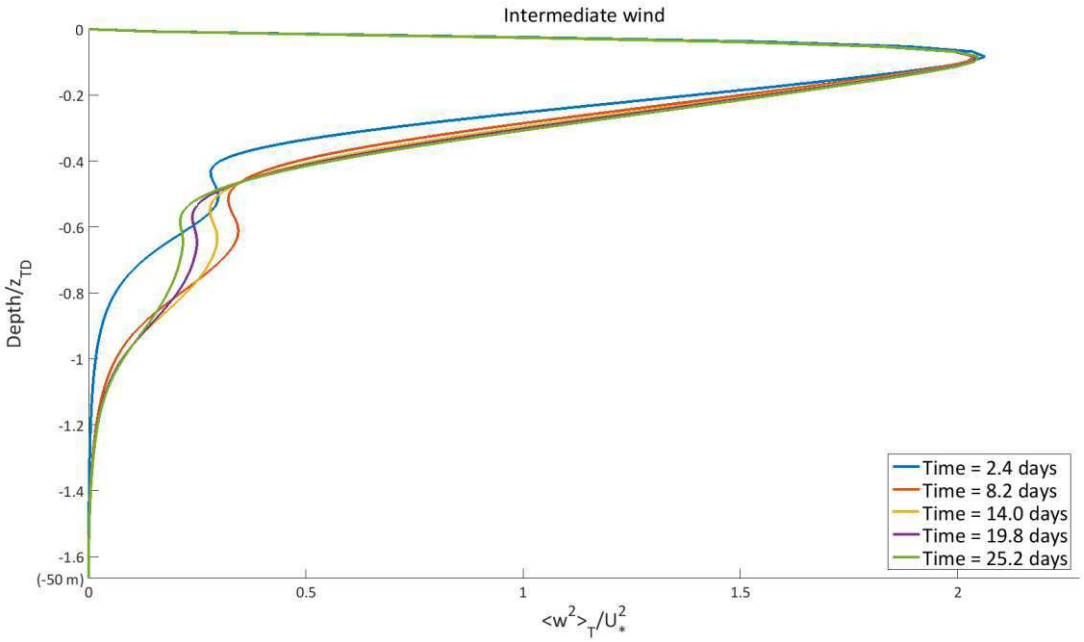
Intermediate wind
Depth/z_{TD}
$\langle w^2 \rangle_T / U_*^2$
Time = 2.4 days
Time = 8.2 days
Time = 14.0 days
Time = 19.8 days
Time = 25.2 days

c

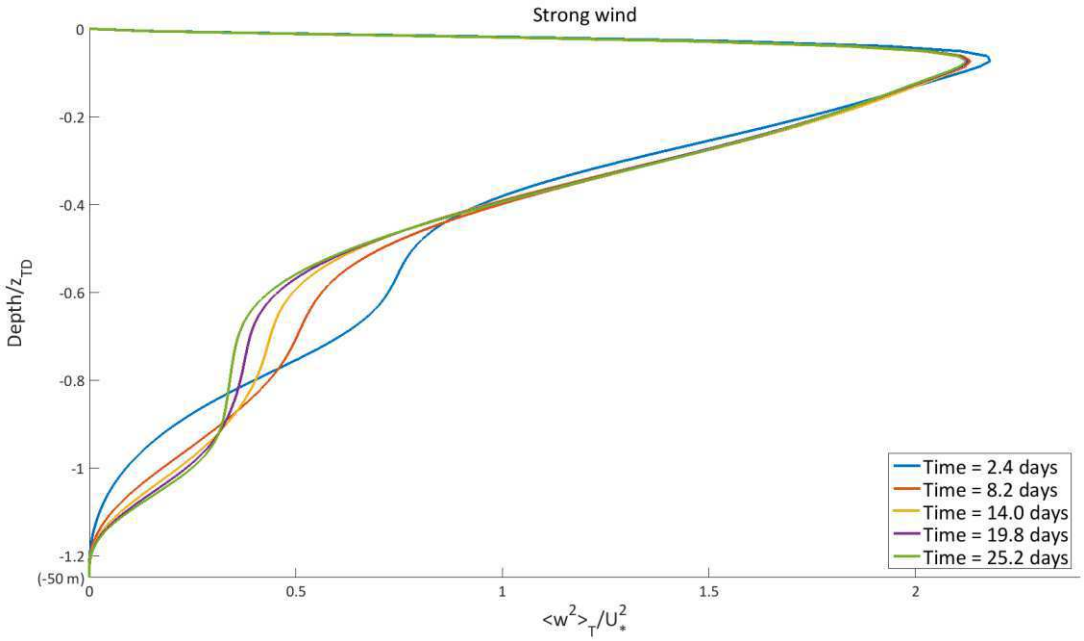
Strong wind
Depth/z_{TD}
$\langle w^2 \rangle_T / U_*^2$
Time = 2.4 days
Time = 8.2 days
Time = 14.0 days
Time = 19.8 days
Time = 25.2 days

Figure 9

a

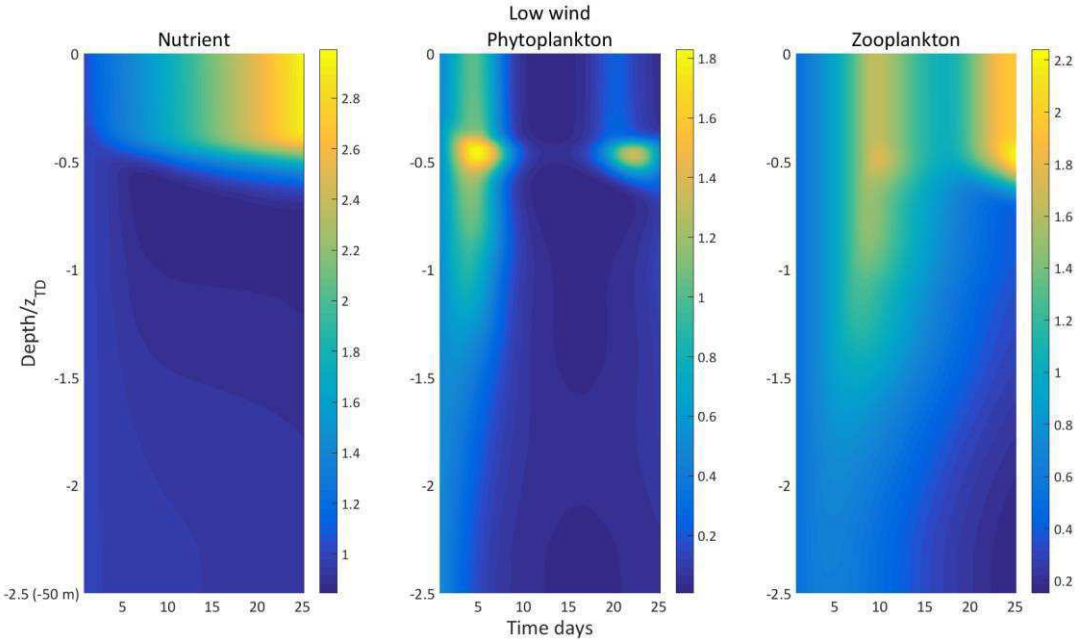

b

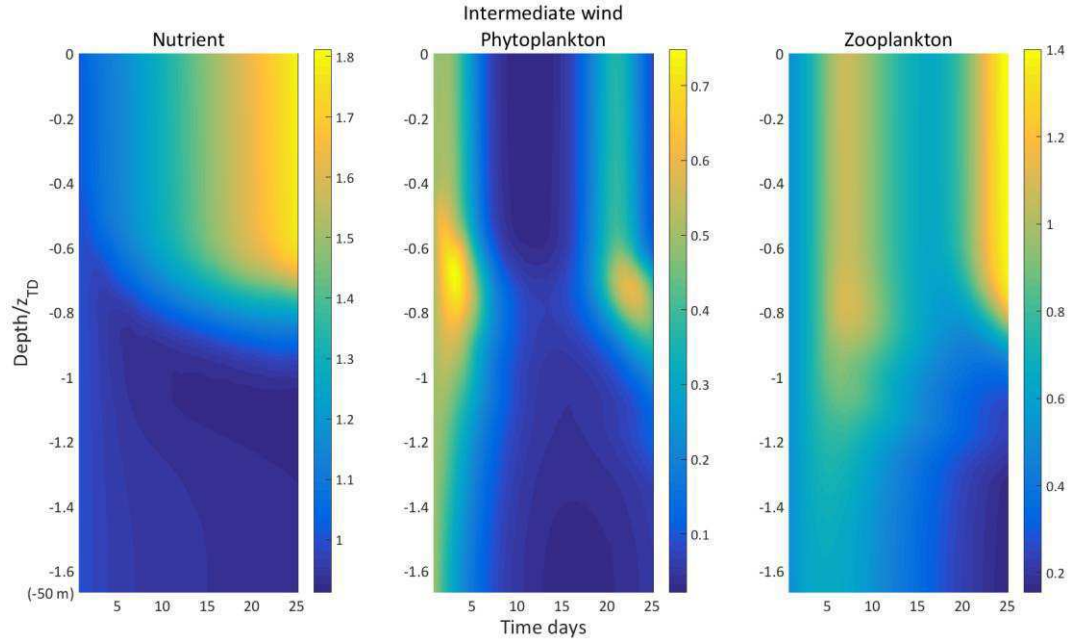

c

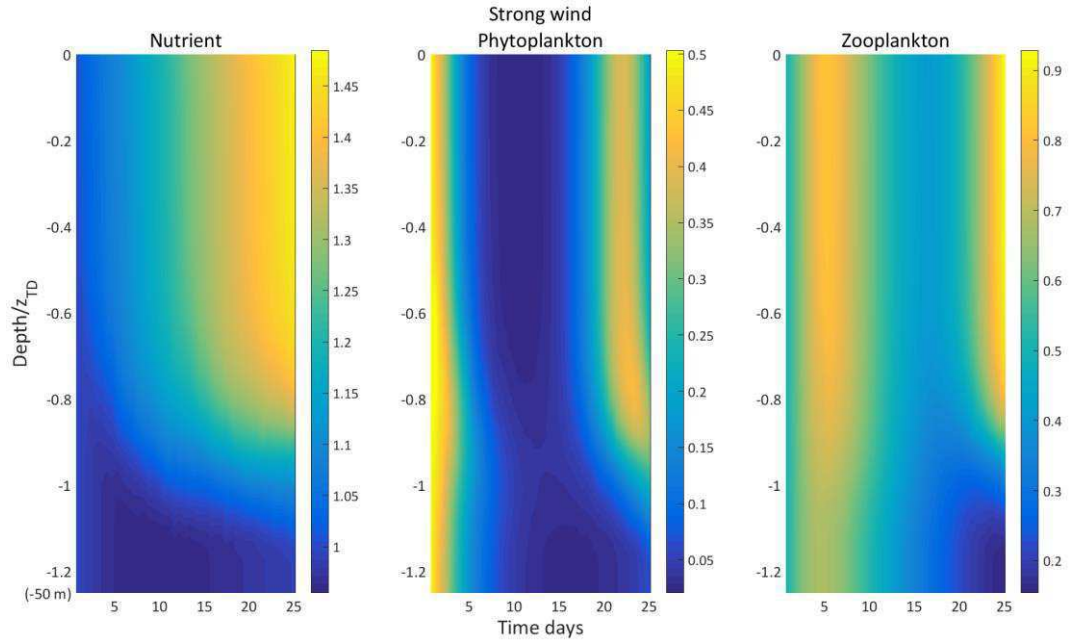

Figure 10

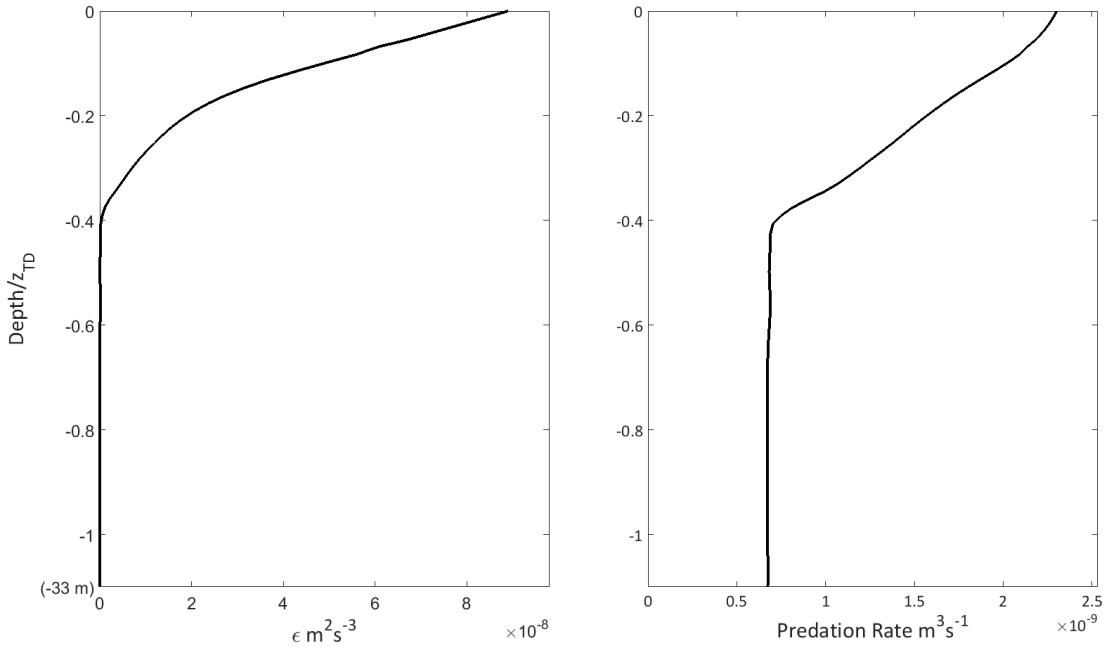

Figure 11

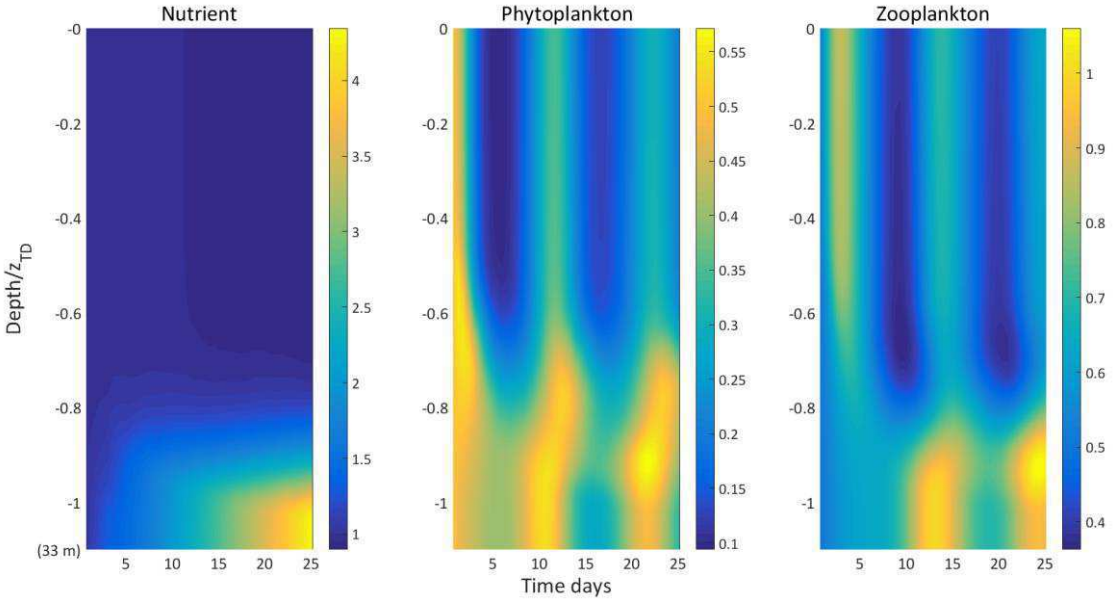

Figure 12

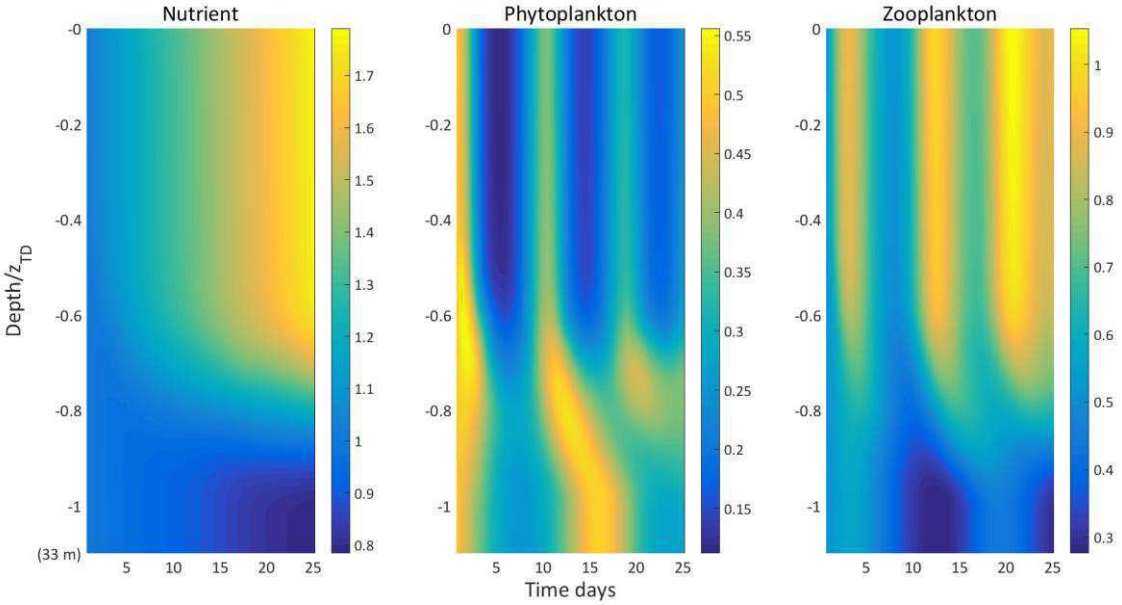

Figure 13

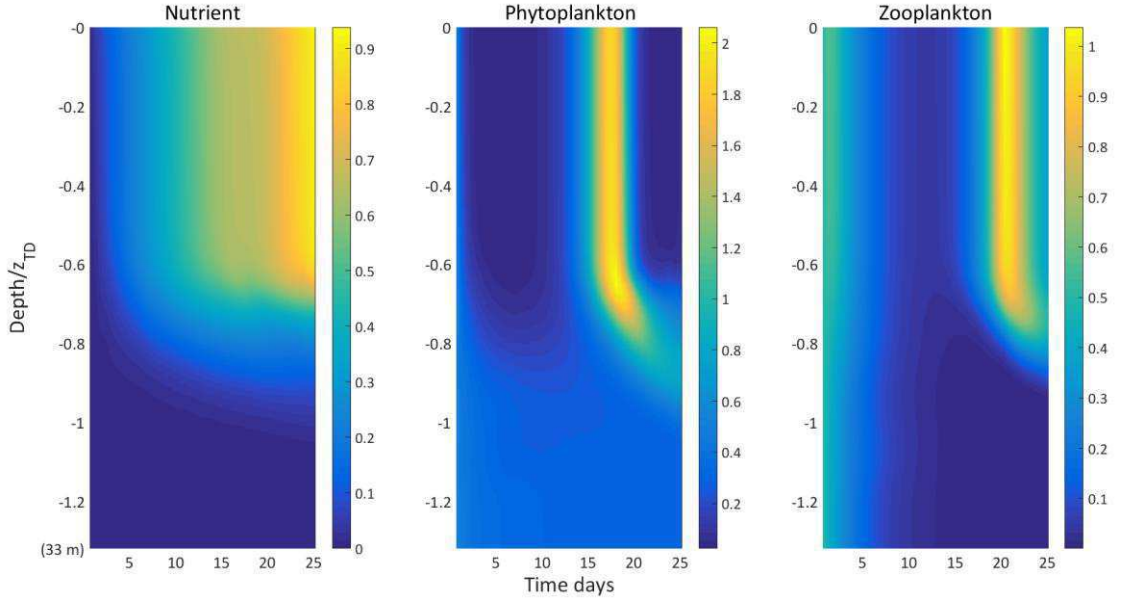

Figure 14

a

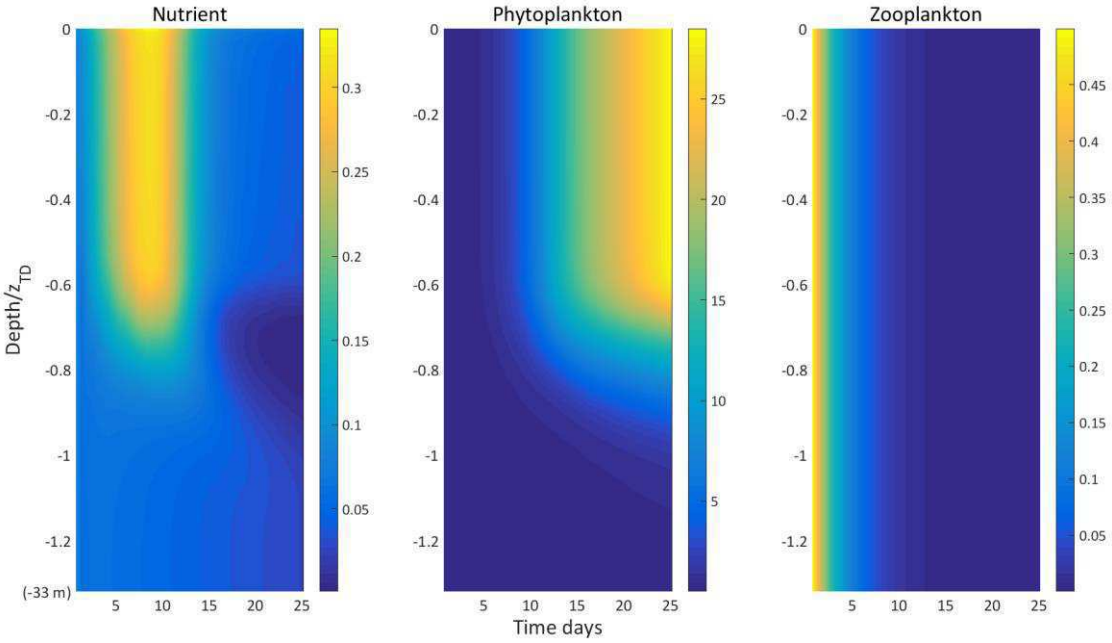
Nutrient
Phytoplankton
Zooplankton
Depth/z_{TD}
Time days
0
-0.2
-0.4
-0.6
-0.8
-1
-1.2
(-33 m)
5
10
15
20
25

b

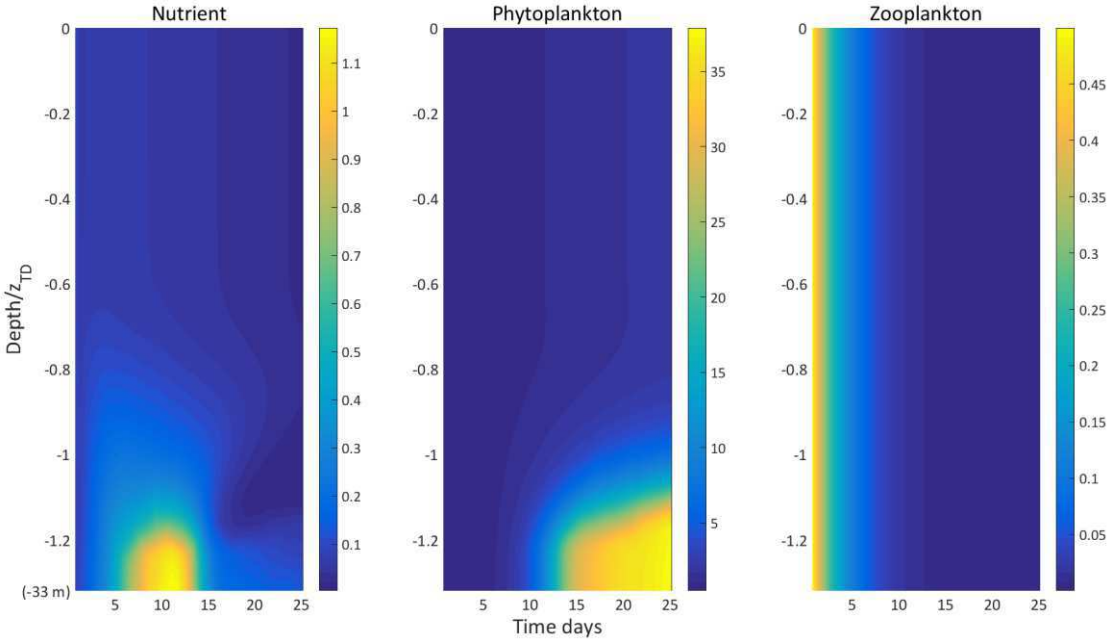
Nutrient
Phytoplankton
Zooplankton
Depth/z_{TD}
Time days
0
-0.2
-0.4
-0.6
-0.8
-1
-1.2
(-33 m)
5
10
15
20
25

Figure 15

a

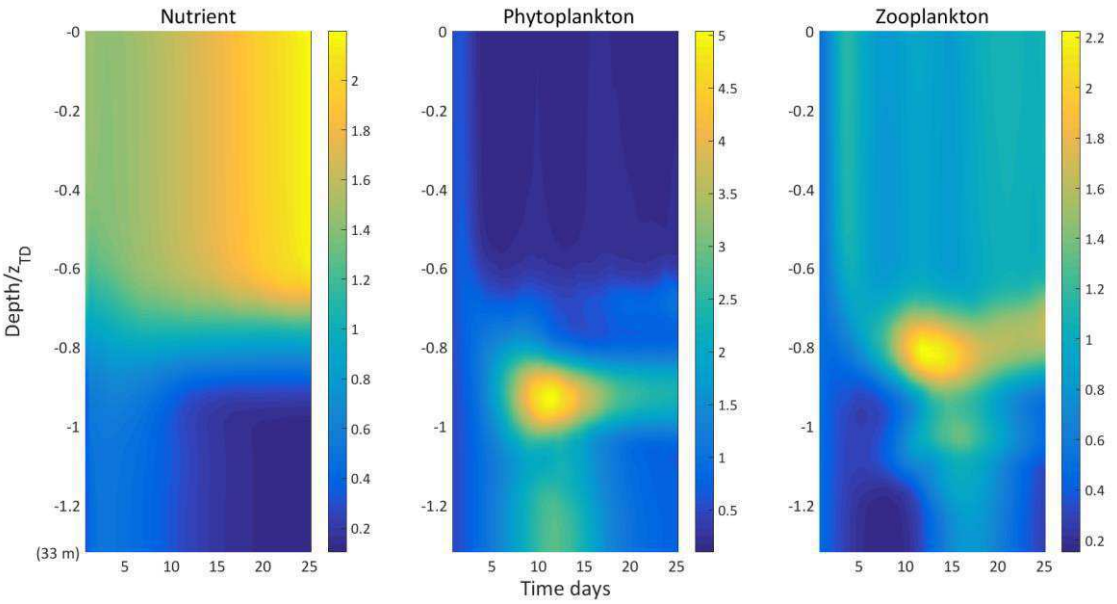
Nutrient
Phytoplankton
Zooplankton
Depth/z_{TD}
(33 m)
Time days

b

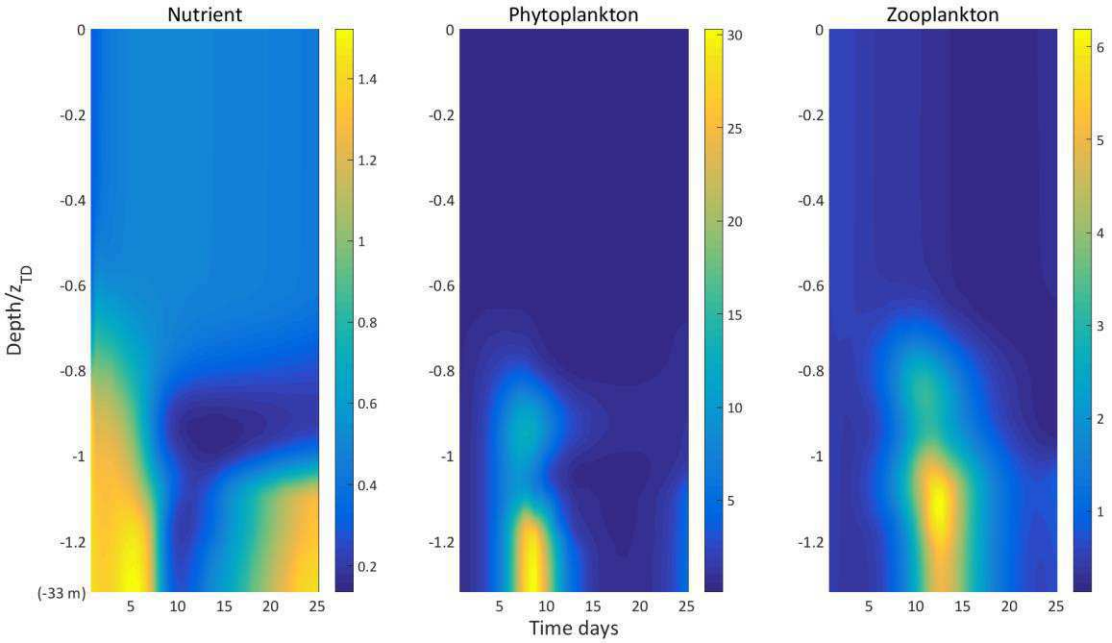
Nutrient
Phytoplankton
Zooplankton
Depth/z_{TD}
(-33 m)
Time days

Figure 16

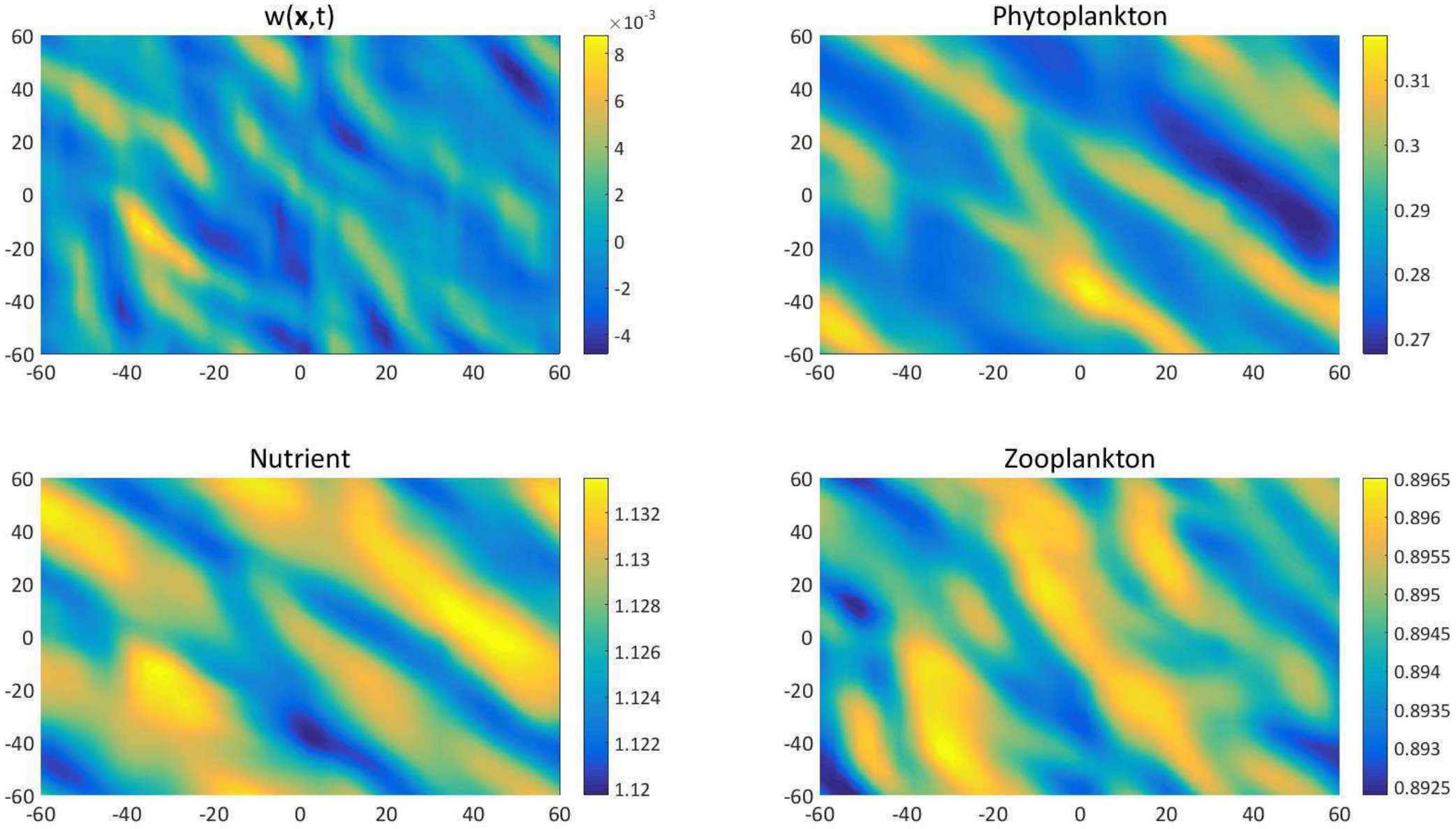
w(x,t)
×10^-3
8
6
4
2
0
-2
-4
Phytoplankton
0.31
0.3
0.29
0.28
0.27
Nutrient
1.132
1.13
1.128
1.126
1.124
1.122
1.12
Zooplankton
0.8965
0.896
0.8955
0.895
0.8945
0.894
0.8935
0.893
0.8925
60
40
20
0
-20
-40
-60

Figure 17

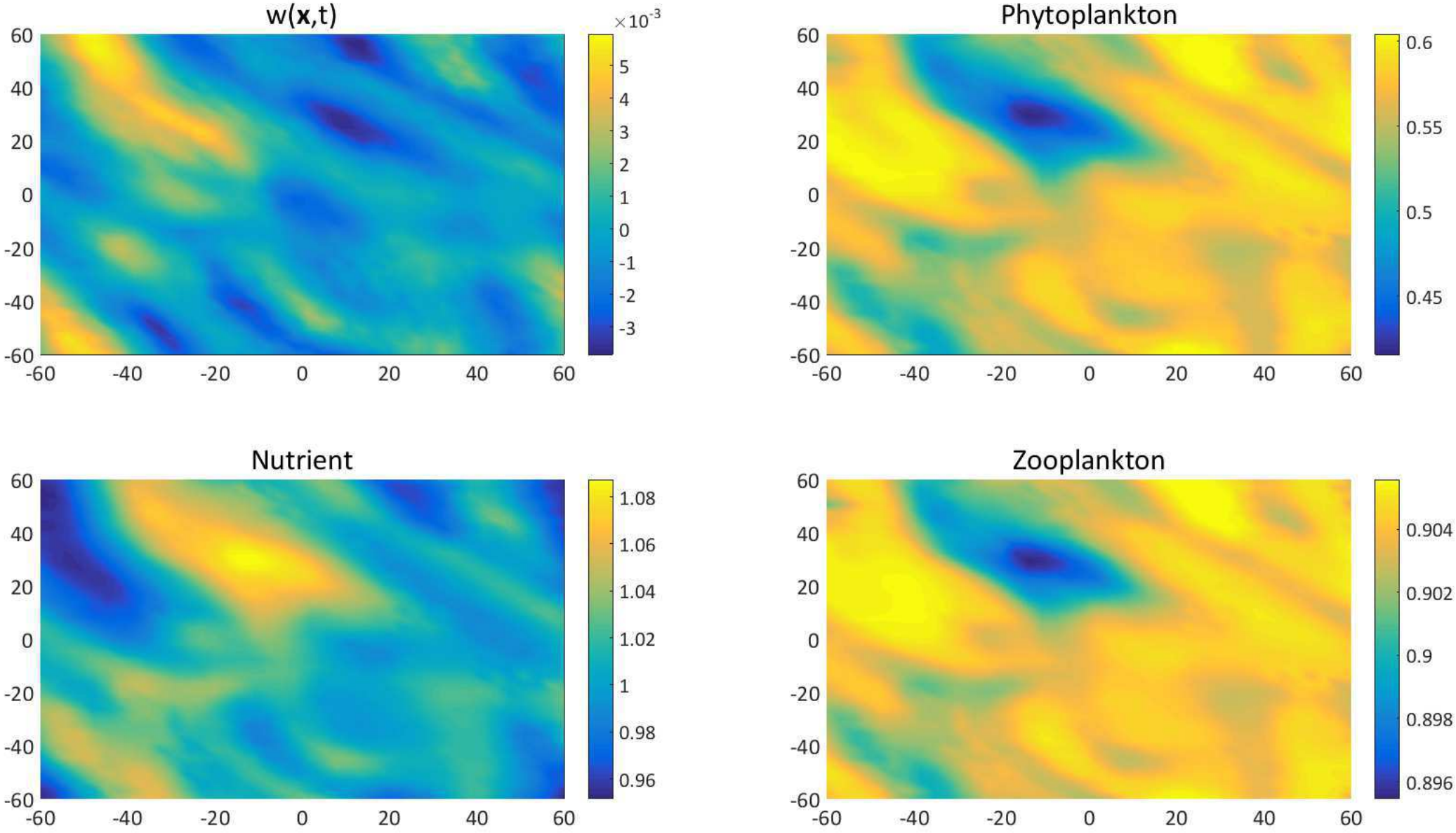
w(x,t)
×10^-3
5
4
3
2
1
0
-1
-2
-3
Phytoplankton
0.6
0.55
0.5
0.45
Nutrient
1.08
1.06
1.04
1.02
1
0.98
0.96
Zooplankton
0.904
0.902
0.9
0.898
0.896
60
40
20
0
-20
-40
-60

Figure 18

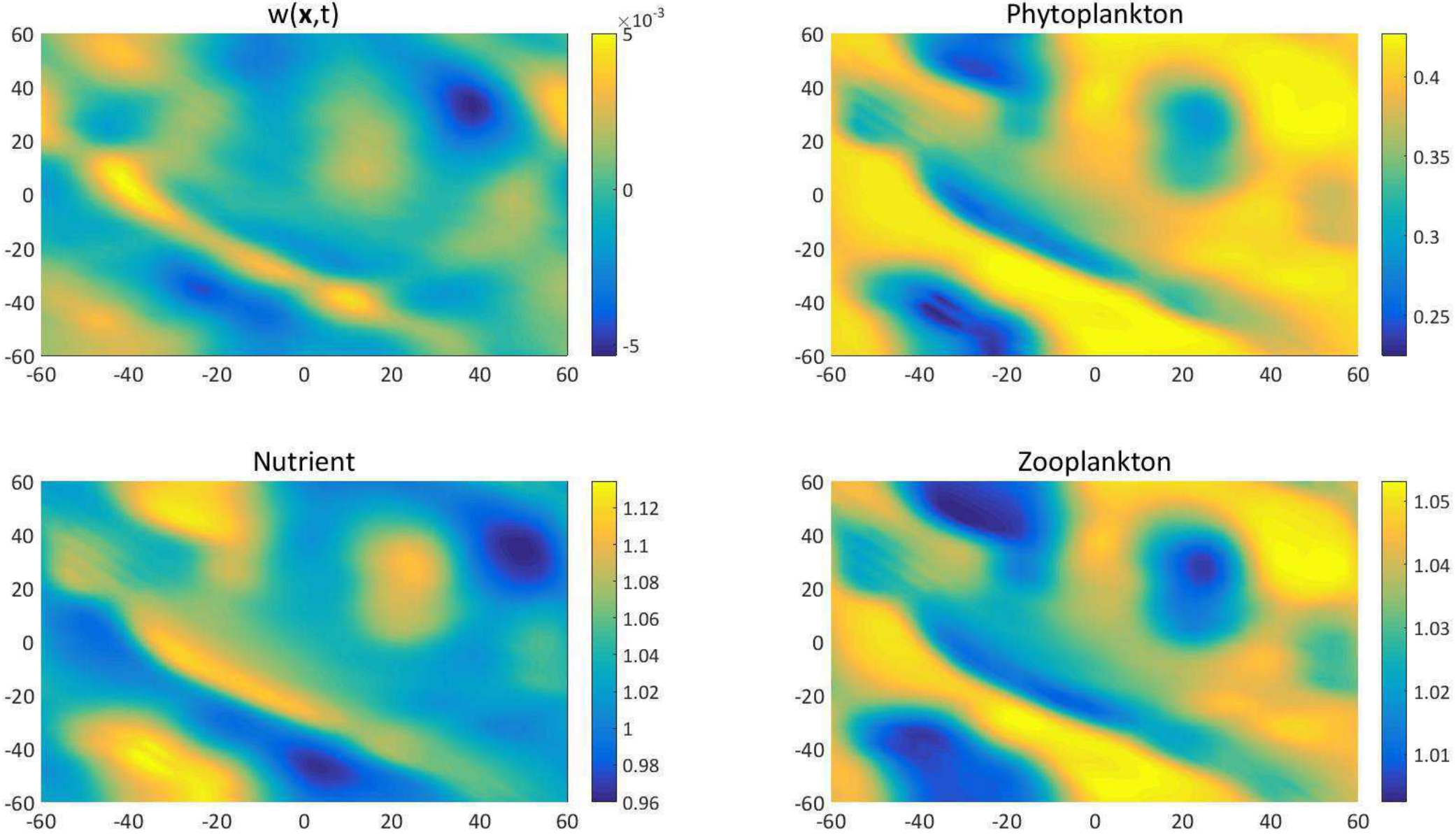
w(x,t)
×10^-3
5
0
-5
Phytoplankton
0.4
0.35
0.3
0.25
Nutrient
1.12
1.1
1.08
1.06
1.04
1.02
1
0.98
0.96
Zooplankton
1.05
1.04
1.03
1.02
1.01
60
40
20
0
-20
-40
-60

Figure 19